Regional CO_2 and CH_4 inversion system using WRF-Chem (v4.4)/DART (v9.8.0) and continuous high-precision observations over the Korean Peninsula

Doyoon Kwon[1], Bonhoon Koo[1], Jooyeop Lee[1], Jeongwon Kim[1], Jaehyung Ahn[1], Jinkyu Hong[1], Eri Saikawa[2], Alexander Avramov[2], Changsub Shim[3], Je-Woo Hong[3], Daegeun Shin[4], Shanlan Li[4], Sumin Kim[4], and Sangwon Joo[4]

[1]Department of Atmospheric Sciences, Yonsei University, Seoul, 03722, Republic of Korea
[2]Department of Environmental Sciences, Emory University, Atlanta, GA, 30319, USA
[3]Korea Environment Institute, Sejong, 30147, Republic of Korea
[4]National Institute of Meteorological Sciences, Jeju-do, 63568, Republic of Korea

Correspondence to: Jinkyu Hong (jhong@yonsei.ac.kr)

Abstract Quantifying greenhouse gas (GHG) emissions over complex terrain remains a significant challenge for conventional inversion systems due to the high sensitivity of tracer transport to surface heterogeneity. We develop a high-resolution dual-species GHG top-down inversion framework by integrating the Weather Research and Forecasting model coupled with Chemistry (WRF-Chem v4.4) and the Data Assimilation Research Testbed (DART v9.8.0) in a cycling ensemble Kalman filter system. Built on community tools, the framework is designed to be portable and configurable, enabling applications to other regions, resolutions, and observing-system configurations (e.g., expanded surface networks and additional data streams). This framework jointly assimilates near-surface CO_2 and CH_4 concentrations to produce dynamically consistent updates of emissions. By employing a unified Eulerian framework that simultaneously updates meteorology and 3-D tracer fields, the system is designed to maintain consistency between transport and concentrations and to reduce the risk that transport-related concentration errors are aliased into flux adjustments over the complex landscapes of the Korean Peninsula. To improve the simulation of turbulent GHG dispersion in the atmospheric boundary layer over complex terrain, we incorporate surface heterogeneity parameterizations (roughness sublayer and canopy height) into the model physics in the inversion system. The system assimilates high-precision continuous *in situ* observations from three World Meteorological Organization/Global Atmosphere Watch (WMO/GAW) stations to constrain CO_2 and CH_4 emissions. Prior flux estimates include anthropogenic emissions (EDGAR v8.0), biogenic exchanges (the region-optimized VPRM), biomass burning (FINN v2.5), and oceanic CO_2 exchanges (SeaFlux). In a 2020 case study, the top-down estimates improve the agreement with ground observations, reducing root-mean-square errors by 30–60 % and lowering posterior mean bias to 1-2 ppm for CO_2 and 20-30 ppb for CH_4 at the high-precision surface observation sites. Independent aircraft profiles provide external evaluation and indicate residual CH_4 discrepancies consistent with prior emissions and boundary condition uncertainties. Controlled observing-system simulation experiments show that, under prescribed perturbations, the system produces bounded and interpretable emission responses to transport-model, boundary-condition, and observation-error perturbations. They also indicate that recovery is strongest within

station footprints and remains coverage-limited under the current three-station network, while a dense-network known-truth experiment highlights the value of expanded observational coverage for improving domain-wide emission constraints. Posterior adjustments suggest reduced CO_2 emissions over the Seoul Metropolitan Area and parts of the western coastal region and increased CH_4 emissions over inland agricultural source regions relative to the priors, highlighting priorities for follow-on evaluation of inventory components. Our posterior CO_2 total (620 ± 45 Mt yr^{-1}) is consistent with the Republic of Korea Biennial Transparency Report (ROK-BTR) estimate (624 Mt yr^{-1}) at the national scale, while the posterior CH_4 total (54.7 ± 5.2 Mt CO_2eq yr^{-1}) exceeds the ROK-BTR estimate (35.5 Mt CO_2eq yr^{-1}) by 19.2 Mt CO_2eq yr^{-1}, consistent with the larger structural uncertainty in CH_4 source characterization and spatial allocation noted in previous studies.

1 Introduction

Anthropogenic emissions of greenhouse gases (GHGs) originate predominantly from fossil fuel combustion, land-use change, agricultural practices, and waste management. These emissions are the principal drivers of contemporary climate change. Reliable and continuous monitoring of anthropogenic GHG emissions is essential for the development of effective climate mitigation strategies, compliance with international climate agreements, and the formulation of informed policy decisions (IPCC, 2021; Friedlingstein et al., 2025). Under the Paris Agreement, national inventories serve as the principal reporting mechanism, delineating Nationally Determined Contributions (NDCs) and facilitating periodic stocktakes (UNFCCC, 2015). These inventories are a standard method within the Measurement, Monitoring, Reporting, and Verification (MMRV) framework and rely on bottom-up methodologies based on activity data and emission factors within a tiered framework established by the Intergovernmental Panel on Climate Change (IPCC) (Ogle et al., 2013). However, their accuracy is often limited by incomplete or outdated activity data, coarse spatio-temporal resolution, diffusive GHG emissions, and systemic delays in updating or reporting inventories (Rogelj et al., 2016; Pauw et al., 2018). Even nations with advanced inventories encounter challenges in capturing rapid emission changes, fine-scale spatial heterogeneity, and localized sources, which undermine the inventory credibility and comparability of inventories (Denison et al., 2019; Nisbet et al., 2019; WMO, 2025).

Top-down approaches, which are based on atmospheric inverse modeling or atmospheric data assimilation (DA), offer independent assessments of emissions by constraining surface fluxes through atmospheric concentration measurements (Enting, 2002; Gurney et al., 2002; Weiss and Prinn, 2011; Oda et al., 2019; Janssens-Maenhout et al., 2020; Elguindi et al., 2020; Mueller et al., 2021; Deng et al., 2022; WMO, 2025). These methodologies are increasingly incorporated into MMRV frameworks (WMO, 2022; 2025). By reconciling observed atmospheric concentrations with emission fluxes, top-down approaches can identify unreported or misrepresented emission sources, detect biases, and provide spatially explicit, policy-relevant emission information (Janssens-Maenhout et al., 2020; Mueller et al., 2021). Recent advancements in observational infrastructure, including dense atmospheric observation networks, satellite platforms, and airborne measurements, have

enabled top-down systems to resolve emission patterns at urban and sub-national scales, thereby enhancing the fidelity and applicability of MMRV systems (Lauvaux et al., 2020; Byrne et al., 2023; Velasco et al., 2023).

Atmospheric inverse modeling frameworks for GHGs differ in how they numerically represent tracer transport. Lagrangian-based approaches release virtual air parcels at receptor sites and track their trajectories backward through prescribed wind fields, reconstructing source-influence functions from the particle paths (e.g., Henne et al., 2016; Pisso et al., 2019; Sijikumar et al., 2023; Brunner et al., 2025; Bukosa et al., 2025). Eulerian approaches instead solve the advection–diffusion continuity equation for tracer mixing ratios on a fixed spatial grid. Within the Eulerian class, global offline systems advect tracers through reanalysis wind, convective mass-flux, and boundary-layer depth fields supplied at each integration step, while regional online-coupled systems such as WRF-Chem integrate the meteorological state and the tracer fields through a single numerical framework, applying the same advection operators, turbulence closures, and planetary-boundary-layer scheme to both. Representation errors in boundary-layer dynamics and sub-grid mixing have been documented across inversion configurations in which meteorology and tracer transport are treated through separate numerical pipelines (Bréon et al., 2015; Lauvaux et al., 2016; Dekker et al., 2017; Super et al., 2017; Gaudet et al., 2021; Nalini et al., 2022; Bukosa et al., 2025). Online-coupled integration yields temporal and sub-grid consistency between the resolved flow and the simulated GHG evolution, which is particularly suited to ensemble-based DA techniques (Kang et al., 2012; Gaudet et al., 2021), including the Ensemble Adjustment Kalman Filter (EAKF) (Anderson, 2001, 2003).

These considerations motivate the development and documentation of complementary high-resolution Eulerian DA frameworks that can explicitly represent mesoscale transport and boundary-layer mixing over heterogeneous surfaces and can be extended to future dense observing systems. The Weather Research and Forecasting model coupled with Chemistry (WRF-Chem) provides high-resolution, online coupling of meteorology and chemistry, while the Data Assimilation Research Testbed (DART) offers an ensemble-based DA platform for dynamically updating meteorological and chemical states. Accordingly, WRF-Chem coupled with the DART has been used in CO_2 concentration, regional meteorology and air quality studies (e.g., Mizzi et al., 2018; Ma et al., 2020; Zhang et al., 2021a). Previous studies have demonstrated the feasibility of coupling WRF-Chem with DART for CO_2 flux inversion using satellite XCO_2 retrievals in an ensemble Kalman filter framework (Zhang et al., 2021a; 2021b; Jin et al., 2025).

While these studies establish feasibility, they have primarily focused on single-species CO_2 estimation constrained by intermittent satellite sampling, and the extent of independent flux evaluation (e.g., using independent *in situ*/aircraft constraints) and controlled sensitivity testing remains relatively limited for comprehensive flux-inversion assessment. Furthermore, applications to CO_2 and CH_4 regional inversions at kilometer-scale transport resolution remain limited particularly in complex-terrain environments where transport–flux aliasing and representativeness errors can be substantial. To our knowledge, a fully documented WRF-Chem/DART regional inversion framework that simultaneously targets CO_2 and CH_4 emissions and assimilates both *in situ* GHG observations and meteorological fields within a cycling dual-state configuration has not yet been documented in the literature. The present study fills this gap by providing a reproducible dual-species (CO_2/CH_4) state-augmentation system with explicit configuration choices, including uncertainty assumptions, localization/inflation,

observation selection, boundary condition handling, together with a real-data application and a supplementary set of controlled OSSEs spanning transport-model, and observation-error/representativeness perturbations with real-case diagnostics of ensemble-size sensitivity and inflation-related spread consistency.

Here we extend the WRF-Chem (v4.4) and DART (v9.8.0) framework to implement a 9-km dual-species inversion system that cycles meteorological DA while assimilating near-surface CO_2 and CH_4 observations, directly updating meteorology and 3-D tracer fields and estimating surface flux adjustments through ensemble cross-covariances. We further incorporate surface-heterogeneity-related physics and land information (e.g., roughness-sublayer and canopy-height adjustments) tailored to the Korean Peninsula, where complex topography, coastal circulations, clustered emissions, and monsoon seasonality pose challenges for conventional inventories and coarse-resolution inversions (e.g., Hong and Kim, 2011; Hong et al., 2019; Hong et al., 2020; Lee et al., 2021; Kim et al., 2024). The main practical assessment is based on the 2020 real-data application, using concentration-space diagnostics, flux uncertainty reduction, independent aircraft observations, and intercomparisons with multiple emission datasets to evaluate the framework's relevance for future national MMRV-oriented applications.

2 Description of CO_2 and CH_4 inversion framework

2.1 Atmospheric modeling system

Our GHG inversion framework integrates a regional Eulerian atmospheric chemistry model with an ensemble-based data assimilation system. Specifically, this framework employs the Weather Research and Forecasting model coupled with Chemistry (WRF-Chem v4.4; Grell et al., 2005) and the Data Assimilation Research Testbed (DART v9.8.0) (Anderson et al., 2009) for sequential data assimilation. WRF-Chem solves the fully compressible, nonhydrostatic Eulerian equations on a fixed spatial grid, and simulates atmospheric dynamics, physical and chemical processes, and chemical transport within a unified framework.

In the inversion system, WRF-Chem generates ensemble forecasts by simulating meteorology with surface fluxes and atmospheric transport processes of GHGs. Given the long atmospheric lifetime of GHGs, they have been simulated as passive tracers in mesoscale models (Dekker et al., 2017; Super et al., 2017; Zhao et al., 2023). WRF-Chem includes the module to simulate passive tracer transport of GHGs since WRF-Chem v3.4 (Beck et al., 2012). In WRF-Chem, distinct variables represent background, anthropogenic, biomass-burning, oceanic (CO_2 only), and biogenic components of CO_2 and CH_4. The model simulates their fluxes, transport, and diffusion processes driven by the meteorological field to obtain a three-dimensional concentration field on an hourly basis. The total concentrations are represented as the sum of the component variables, facilitating comparison with observed concentrations. CO_2 and CH_4 are treated as passive tracers for our regional application because the relative chemical lifetime of CH_4 against OH is on the order of years (about 9 years), whereas typical air-mass residence times across our regional domain are <1 day (Zhao et al., 2020; Callewaert, 2024). Therefore, the implied fractional loss is negligible compared to transport and emission uncertainties. In addition, large-scale chemical aging and seasonality are already reflected in the prescribed initial and lateral boundary conditions.

Our study area consists of a single model domain with 9-km horizontal spacing of 97 × 136 grid points and 51 terrain-following vertical levels stretching from the surface up to 50 hPa at the upper boundary (Fig. 1). The model employed specific physics parameterization schemes (Kim et al., 2024 and references therein), including the WSM-6 microphysics, Rapid Radiative Transfer Model for General Circulation Models (RRTMG) shortwave and longwave radiation schemes, the Yonsei University scale-aware Planetary Boundary Layer (PBL) scheme, Kain-Fritsch cumulus scheme, and the Unified Noah Land Surface Model (LSM).

Notably, for better simulations of GHG transport over complex terrain, we used the revised WRF-Chem by replacing the default WRF canopy height with high-resolution (1 km) spaceborne lidar-retrieved canopy height data (GLAS/ICESat) for a better representation of surface characteristics (Lee and Hong, 2016). To simulate realistic transport and dispersion of GHG in the PBL, we further adapted roughness sublayer (RSL) parameterization of Lee et al. (2020), which incorporated the RSL function from the unified theory of Harman and Finnigan (2007, 2008) and Harman (2012), into the revised MM5 surface layer scheme (Jiménez et al., 2012) and Unified Noah LSM in WRF. Hereafter, we refer to this modified WRF-Chem v4.4 as WRF-Chem GHG.

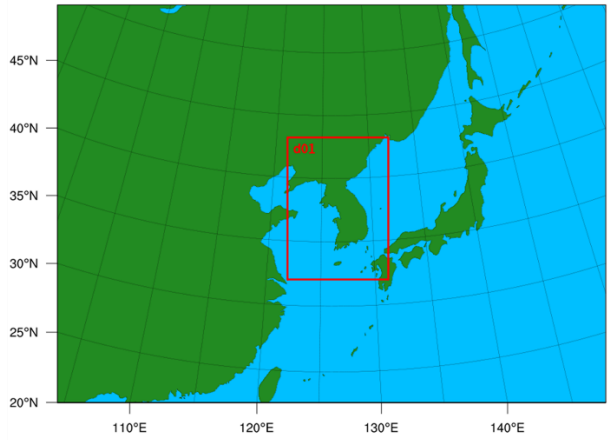

Figure 1. The WRF-Chem domain configuration used in this study.

2.2 DART data assimilation for GHG inversion

DART serves as a modular DA system designed to interface with various atmospheric models and observational datasets. The integration of WRF-Chem and DART enables the simultaneous assimilation of meteorological variables and chemical species through multivariate, dynamically consistent updates across the coupled system (Mizzi et al., 2016; Mizzi et al., 2018). The system operates as an ensemble of WRF-Chem forecasts, where each member represents a perturbed version of the state vector that accounts for both observational and model uncertainties. At each analysis cycle, ensemble perturbations are utilized to estimate a flow-dependent background error covariance, enabling the EAKF to adjust both meteorological and tracer fields

simultaneously in a dynamically balanced manner. This ensemble-based structure allows for uncertainty propagation, sequential updating of the background (prior) ensemble, and the maintenance of consistency between state variables during sequential assimilation. Hereafter, we refer to WRF-Chem GHG coupled with DART as WRF-Chem/DART.

Our work extends the DA system to facilitate the simultaneous assimilation of observed CO_2 and CH_4 concentrations with meteorological data at a spatial resolution of 9 km over the Korean Peninsula. The assimilated data include continuous *in situ* CO_2 and CH_4 concentrations, alongside standard meteorological observations from National Centers for Environmental Prediction (NCEP) automated data processing upper air and surface observations (PREPBUFR observations). Because meteorology is simulated and updated within the online WRF-Chem/DART cycling system (rather than prescribed as offline transport fields), the inversion does not rely on externally prescribed meteorological trajectories. Meteorological initial and boundary conditions (IC/BCs hereafter) are provided from standard large-scale reanalysis products as in limited-area modeling.

We use an ensemble size of 20 members throughout the cycling assimilations in the WRF-Chem/DART system. A real-case simulations with 10, 20, and 30 members shows that the 20- and 30-member configurations behave similarly in terms of the prior RMSE/total-spread ratio, supporting the 20-member choice as a practical compromise between covariance sampling and computational cost (Supplement Sect. S3.1, Fig. S23). The analysis directly updates the prognostic meteorological variables and 3-D tracer concentration fields each cycle, while emission adjustments are estimated as surface forcing parameters for the subsequent forecast, rather than being dynamically transported like tracer concentrations. This cycling approach helps preserve meteorology–transport–concentration consistency between the analyzed meteorology/tracer fields and the subsequent model transport in the ensemble forecasts. In the sequential EAKF framework, correcting the tracer concentration state at each analysis step (e.g., using the analysis field as the initial condition for the subsequent forecast) helps prevent the carry-over of transport-driven concentration biases and reduces the risk that these biases are aliased into inferred emission adjustments. As demonstrated in previous WRF-Chem/DART studies (Liu et al., 2017; Hsu et al., 2024), failure to correct the concentration state allows transport-driven biases to persist into subsequent forecast steps. The filter would then continuously interpret these persistent concentration residuals as evidence of flux errors, leading to the artificial amplification of emission estimates (over-adjustment) to compensate for accumulated biases. For passive tracers such as CO_2 and CH_4, chemical loss is negligible at the cycling timescale, so transport-driven biases accumulate without meaningful attenuation. Similar concentration-state correction is applied in ensemble-based CO_2 flux estimation systems (Kang et al., 2011, 2012; Peng et al., 2015). By updating the concentration state at each cycle, the system ensures that emission adjustments are derived primarily from mismatches between model forecast and observation within the current assimilation window.

We implement this joint state–emission estimation using a state-augmentation approach in DART (Kang et al., 2011, 2012; Liu et al., 2017; Zhang et al., 2021a; Huang et al., 2022). The augmented state vector is defined as:

$$\boldsymbol{z} \equiv \boldsymbol{x} = \left[\boldsymbol{x}_{met}, \boldsymbol{x}_{chem}, \boldsymbol{x}_{flux}\right]^{\mathrm{T}} \quad (1)$$

where $\boldsymbol{x}_{met}$ contains meteorological variables including zonal and meridional wind, temperature, specific humidity, and surface pressure ($U,V,T,Q,$ and P_{sfc} respectively), $\boldsymbol{x}_{chem}$ contains three-dimensional CO_2 and CH_4 mixing ratios, and $\boldsymbol{x}_{flux}$ contains two-dimensional surface emission flux fields and is represented as time-indexed (e.g., hourly) flux fields that are applied as external surface-forcing inputs to WRF-Chem during the subsequent forecast integration. At each analysis time, the deterministic EAKF updates the prior (background) augmented-state ensemble to the posterior ensemble:

$$\bar{z}^u = \mathbf{\Sigma}^u \left[(\mathbf{\Sigma}^p)^{-1} \bar{z}^p + \mathbf{H}^{\mathrm{T}} \mathbf{R}^{-1} \boldsymbol{y}^o \right] \tag{2}$$

$$\mathbf{\Sigma}^u = \left[(\mathbf{\Sigma}^p)^{-1} + \mathbf{H}^{\mathrm{T}} \mathbf{R}^{-1} \mathbf{H} \right]^{-1} \tag{3}$$

$$z_i^u = \mathbf{A}\left(z_i^p - \bar{z}^p \right) + \bar{z}^u, \qquad i = 1, \ldots, N \tag{4}$$

where $\bar{z}^u$ and $\bar{z}^p$ denote the posterior and prior ensemble means, respectively. The subscript i in z_i^p and z_i^u indicates the i-th member of the prior/posterior ensembles, and N is the ensemble size. $\boldsymbol{y}^o$ is the observation vector including *in situ* CO_2/CH_4 and PREPBUFR meteorological observations, $\mathbf{R}$ is the observation-error covariance matrix, and $\mathbf{H}$ is the corresponding observation (forward) operator. $\mathbf{\Sigma}^p$ and $\mathbf{\Sigma}^u$ are the prior and posterior error covariance matrices, respectively. $\mathbf{A}$ is a transformation matrix satisfying $\mathbf{\Sigma}^u = \mathbf{A}\mathbf{\Sigma}^p\mathbf{A}^{\mathrm{T}}$, consistent with the EAKF adjustment used here. Equations (2) and (3) provide a compact summary of the linear Kalman analysis. In practice, DART implements the EAKF as a deterministic, serial ensemble update in observation space, where each observation is assimilated sequentially using ensemble-estimated covariances with covariance localization. The ensemble adjustment matrix $\mathbf{A}$ in Eq. (4) is computed so that the posterior ensemble anomalies reproduce the localized posterior covariance in Anderson (2001, 2003), thereby avoiding the sampling noise associated with stochastic perturbations of observations. We refer to Anderson (2001, 2003) and Anderson et al. (2009) for the detailed mathematical and theoretical backgrounds for EAKF.

For *in situ* CO_2 and CH_4, we specify the observation error variance as $\sigma^2 = \sigma^2_{\mathrm{meas}} + \sigma^2_{\mathrm{repr}}$, where σ^2_{meas} is the measurement uncertainty reported for the WMO/GAW stations (Lee et al., 2019; Lee et al., 2023) and σ_{repr} is treated as a model–data mismatch term, not as an instrument error, and its magnitude is chosen to maintain stable cycling behavior and to avoid overfitting sparse point observations in a 9-km grid framework. Because σ^2_{meas} is expected to be small for WMO/GAW-quality observations, σ_{repr} is treated as the primary contributor and is parameterized as a concentration-proportional term (as 5 % of the observed mole fraction) across all sites. This results in a relatively large effective error variance (typically ~20 ppm for ambient CO_2 and ~100 ppb of CH_4). This conservative parameterization is chosen not only to account for sub-grid variability but also to maintain analysis stability given the sparsity of the operational network. In data-sparse regions, relying too heavily on individual stations (via small observation errors) risks introducing spurious emission artifacts driven by local transport transients; a larger error specification mitigates this risk by ensuring that increments are driven only by persistent, robust

signals. For PREPBUFR meteorological observations, we use the DART default observation error specifications based on the NCEP operational error tables (e.g., rawin wind: 1.4–3.2 m s^{-1}, radiosonde temperature: 0.8–1.5 K, land station wind: 3.5 m s^{-1}, marine wind: 2.5 m s^{-1}, surface pressure: 1.0 hPa), which are platform- and pressure- (altitude) dependent. The synthetic-observation errors used in the controlled OSSEs are specified separately in Supplement S2 to impose prescribed observation-error perturbations of known magnitude; they are therefore controlled sensitivity settings rather than a direct restatement of the real-data representativeness-error parameterization.

Although the surface emission fluxes $\boldsymbol{x}_{flux}$ are not directly observed (i.e., **H** has no sensitivity to fluxes), they are updated through the ensemble cross-covariances $\mathrm{Cov}(\boldsymbol{x}_{chem}, \boldsymbol{x}_{flux})$. These flow-dependent covariances enable statistically consistent flux adjustments that reduce concentration innovations, provided that physically plausible concentration–flux relationships exist within the localization radius. The updated emission fields are prescribed as static surface inputs that persist during the subsequent forecast window, rather than being advected as prognostic variables. Thus, the emission corrections obtained at each analysis cycle propagate forward through the forecast into the next analysis cycle. To suppress sampling error and spurious long-range correlations, we apply covariance localization using a Gaspari–Cohn polynomial with a horizontal half-width of 0.025 rad (~ 160 km) and a vertical normalization cutoff radius of 1.5 km, constraining increments primarily to the lower troposphere and reducing under-sampling error (Gaspari and Cohn, 1999; Anderson, 2012; Kang et al., 2012). Cross-species covariances are not applied; CO_2 and CH_4 tracers are updated independently. To mitigate ensemble under-dispersion, we apply adaptive prior inflation in DART (*inf_flavor* = 2). The inflation standard deviation is initialized at 0.6 and damped by a factor of 0.9, with the maximum allowed change per cycle limited to 1.05. A real-case comparison of three adaptive-inflation configurations, including prior-only and prior-and-posterior Gaussian schemes and a prior-only inverse-gamma scheme, yields nearly identical prior RMSE/total-spread ratios at the observation sites, indicating comparable concentration-space spread consistency under the tested configurations (Fig. S24). This diagnostic does not imply that posterior emissions are insensitive to inflation settings, because emission increments also depend on emission-state spread and concentration–emission cross-covariances.

Prior uncertainty is represented by applying Gaussian, multiplicative perturbations to the chemical initial state, lateral boundary conditions, and anthropogenic emission fluxes when generating the forecast ensemble. For each ensemble member, perturbation factors are drawn from normal distributions centered at unity, with 1σ standard deviations of 5% for chemical initial and lateral boundary conditions and 30% for anthropogenic fluxes. The former represents a pragmatic balance between acknowledging residual uncertainty in the reanalysis inflow and preventing ensemble over-spreading that would overwhelm regional increments, while the latter is chosen to span the inter-inventory discrepancies over the Korean Peninsula (see Section 6.4 for details). The initial error configurations also align with those from previous studies (e.g. Zhang et al., 2021a, b). Horizontal and vertical correlation lengths are specified as 200 km and 1 km, respectively.

Analyses are produced every six hours (00, 06, 12, 18 UTC) using observations within a ±3 h window centered on the analysis time; observations are rejected if they exceed three standard deviations of the background ensemble. The resulting analyzed ensemble is then advanced with WRF-Chem to provide the background for the next cycle, updating the chemical and

meteorological initial conditions accordingly. To maintain dynamical consistency near the domain boundaries, the analysis increments are propagated consistently into the lateral boundary tendencies used for the subsequent forecast, preventing spurious discontinuities at the boundary interface. This is a numerical continuity treatment and does not constitute an independent optimization of boundary inflow.

A controlled evaluation of the inversion is provided in Supplement S2. The revised Supplement first presents an S1 error-source matrix in which the CTL known-truth retrieval serves as the baseline and prescribed perturbations are introduced for transport-model error, boundary-condition bias, observation-error/representativeness sensitivity, localization radius, and their combination (Table S2, Figs S15–S19) (Michalak et al., 2017; Bisht et al., 2023). These experiments are controlled diagnostics of the implemented state-augmentation system rather than demonstrations of real-world flux accuracy. Under the tested perturbations, the system produces bounded and interpretable emission responses: the structural-error experiments change the domain-mean recovery by less than about 2 percentage points of the prior, whereas the localization sweep produces somewhat larger but still bounded changes. Supplement S2 then presents a separate dense-network known-truth experiment as an idealized information-content diagnostic for expanded observational coverage (Figs S20–S22), and Supplement S3 provides real-case diagnostics of ensemble-size and inflation-configuration sensitivity (Figs S23–S24). Together, these tests characterize the current configuration, identify coverage-limited recovery as a key uncertainty, and motivate future observing-system expansion and assimilation-window sensitivity tests.

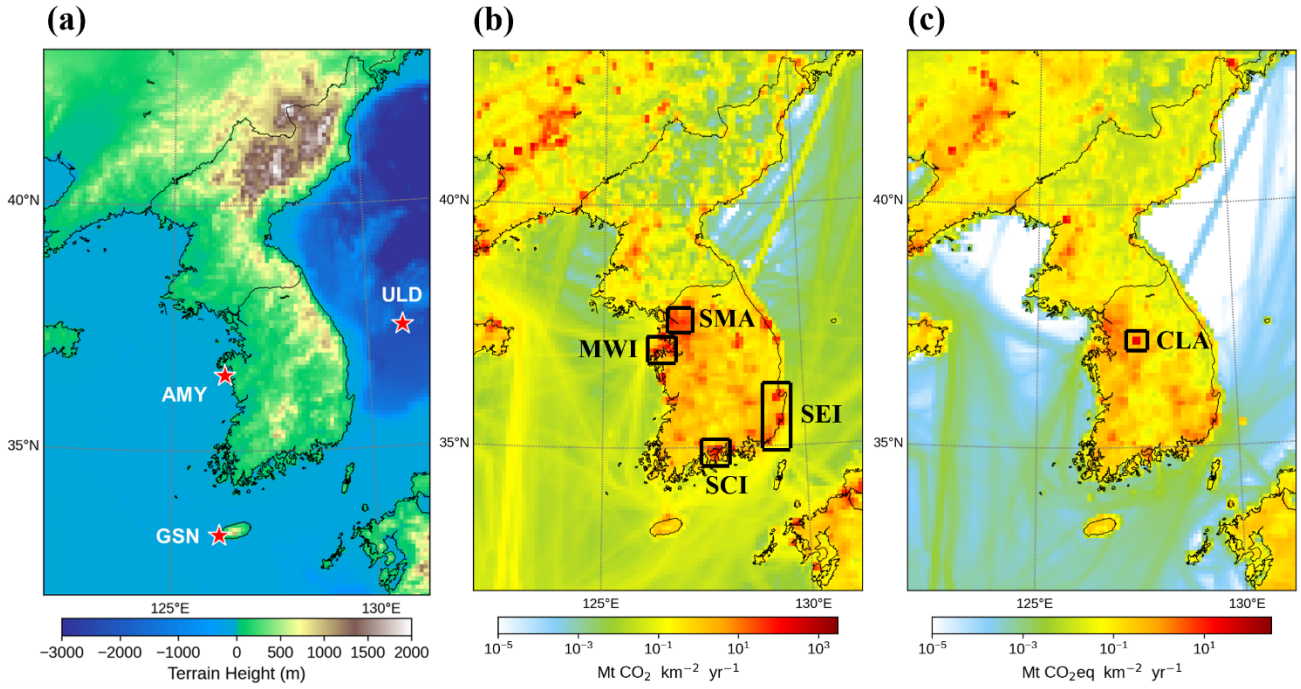

Figure 2. Locations of GHG monitoring stations (AMY, GSN, ULD) over terrain height (a) and annual anthropogenic emissions of CO_2 (b) and CH_4 (c) in the model domain in 2020 from EDGAR (v8.0). Main emission source regions in the model domain are boxed:

SMA (Seoul Metropolitan Area), MWI (Mid-Western Industrial Area), SEI (Southeastern Industrial Area), SCI (South Coast Industrial Area), and CLA (Central Livestock Area).

3 Observation data of GHG concentrations and meteorological conditions for data assimilation

High-precision, continuous ground-based GHG measurements are essential for capturing high-frequency variability and providing constraints on regional enhancements near major source regions. To constrain CO_2 and CH_4 fields, the inversion framework assimilates *in situ* measurements of CO_2 and CH_4 concentrations from the WMO/GAW-affiliated monitoring stations at Anmyeondo (AMY), Gosan, Jeju Island (GSN), and Ulleungdo (ULD) operated by the Korea Meteorological Administration (KMA) (Fig. 2a). Depending on wind direction and atmospheric stability, these sites measure background inflow and downwind plumes from key emission source regions (Fig. 2b and 2c). We therefore retain pollution events (no background selection) and rely on the coupled transport and localization to attribute information primarily within these key source regions.

Each site employs a harmonized measurement system based on cavity ring-down spectroscopy (CRDS, Picarro Inc., USA), paired with a custom cryogenic drying system jointly developed by KMA and the Korea Research Institute of Standards and Science. This setup ensures high-precision CO_2 and CH_4 measurements with minimal water vapor interference, critical for ensuring data quality under Korea's seasonally variable meteorological conditions. Data are collected at 1-minute intervals, processed hourly into Level-2 quality-assured products. Here, Level-2 denotes QA/QC screening and calibration processing, distinct from 'background-selected' products that apply additional baseline selection. All stations are operated as GAW monitoring stations with documented QA/QC and are used here to constrain regional-scale enhancements rather than micro-scale local fluxes. It is worth noting that this Level-2 dataset excludes instrumental artifacts (e.g., calibration periods) but retains local and regional pollution events without applying background selection filters, ensuring that the high-concentration signals required for regional inversion are preserved. Further details on instrument calibration, QA/QC protocols, and traceability to international standards for CO_2 and CH_4 observations at WMO/GAW sites in Korea can be found in Lee et al. (2019) and Lee et al. (2023), respectively.

The new surface parameterizations adopted in this study improve wind simulations near the surface (e.g., Lee et al., 2015; Lee and Hong, 2016; Lim et al., 2019; Lee et al., 2020; Lee et al., 2023; Kim et al., 2024; Jo et al., 2025; WMO, 2025). For reference, we provide concise verification of modeled 10-m winds with KMA's Automated Synoptic Observing System (ASOS) observations at Seosan (~32 km NNE of AMY), ULD, and GSN, complemented by a comparison against the marine meteorological observation buoy ~18 km east of ULD (Fig. S1–S2 and Table S1). At ULD (a steep volcanic island in open ocean, ~73 km² in area with a peak rising to ~984 m, comparable in extent to a single grid cell), the model exhibits relatively large wind errors that the grid cannot fully resolve; the buoy comparison shows substantially better model agreement with the

surrounding marine wind field, while indicating a possible discrepancy related to local topographical representativeness rather than systematic regional transport bias.

In addition, we assimilate conventional meteorological observations from the NCEP PREPBUFR datasets. These include surface pressure, near-surface air temperature, wind speed and direction, and specific humidity, as well as sea surface temperature and upper-air wind observations (including satellite-derived winds, radiosonde soundings, and aircraft reports of winds, temperature, and humidity). Assimilating these data effectively constrains the meteorological state (winds, temperature, and humidity), thereby improving transport fidelity in the coupled WRF-Chem/DART system, consistent with the previous applications (Mizzi et al., 2016; Mizzi et al., 2018; Pouyaei et al., 2023).

4 Initial and boundary conditions for meteorological variables and GHG concentrations

Meteorological initial and boundary conditions are obtained from the hourly ERA5 global reanalysis data at 0.25° × 0.25° resolution (Hersbach et al., 2020; Hersbach et al., 2023a, 2023b). The initial and boundary conditions are preprocessed by the WRF Preprocessing System (WPS) to the model grid and then perturbed by the WRF Data Assimilation System (WRFDA), as described in previous studies (Barker et al., 2012; Mizzi et al., 2016; Liu et al., 2017; Zhang et al., 2021b).

Initial and boundary conditions of CO_2 and CH_4 are provided by the ECMWF CAMS global GHG reanalysis (EGG4 hereafter) data (Inness et al., 2019; Agustí-Panareda et al., 2023). EGG4 applies 4D-Var data assimilation of *in situ* networks and satellite retrievals within the ECMWF's Integrated Forecast System (IFS Cycle 47R1) and currently covers the period of 2003–2020. The dataset provides atmospheric mixing ratios of CO_2 and CH_4, along with meteorological and chemical variables on regular 0.75° × 0.75° grid in 25 pressure levels and 60 hybrid σ-pressure vertical levels at 3-hourly intervals. EGG4 data as initial and lateral boundary conditions help ensure that large-scale seasonal and regional variability and the growing season CO_2 drawdown are represented in the background fields.

Previous evaluations indicate that EGG4 reanalysis data may exhibit systematic biases. Overall errors in CO_2 and CH_4 concentrations are within 10 ppm and 40 ppb near the Earth's surface (Agustí-Panareda et al., 2023). Validation of EGG4 data against Total Carbon Column Observing Network (TCCON) measurement shows standard deviations of the difference of 1.18 ppm for XCO_2 and 11.3 ppb for XCH_4 (Wang et al., 2023). Notably, it has been reported that EGG4 data have a positive bias of CO_2 concentrations in high-emission regions, and its mean bias is about 7.46 ppm in Asia (Custódio et al., 2022). Regional biases can be systematic and location-dependent; for example, a negative bias of about 30 ppb in CH_4 concentration has been reported at the NOAA flask site in the midwestern industrial region (MWI) (Segato et al., 2025). We also note that even though EGG4 accounts for large-scale CH_4 oxidation, it relies on prescribed OH fields (or climatological loss rates) rather than interactive chemistry. This parameterized sink can introduce systematic errors in CH_4 concentrations, where the prescribed loss rates fail to capture local and temporal variability in photochemical destruction (e.g., Zhao et al., 2020; Agustí-Panareda et al., 2023). We summarize these boundary-driven bias characteristics as diagnostic context to motivate our boundary-condition uncertainty treatment and to aid the interpretation of residual baseline behavior discussed in Section 6.

5 Prior fluxes

5.1 Anthropogenic emissions

Within the domain, WRF-Chem simulates GHG transport and adds contributions from local surface emissions and sinks. Anthropogenic CO_2 and CH_4 emissions used as prior fluxes are regridded from the EDGAR global GHG emission inventory version 8.0 (Crippa et al., 2023). EDGAR provides anthropogenic emissions data in accordance with IPCC-compliant methodologies based on international activity data and emission factors (Janssens-Maenhout et al., 2019, Crippa et al., 2024). In EDGAR, the sectoral composition differs markedly between CO_2 and CH_4 over South Korea. CO_2 emissions are dominated by the power, energy, and industrial sectors (combustion and processes), with additional contributions from transport, fuel exploitation, and buildings (and minor contributions from remaining sources). In contrast, CH_4 emissions are dominated by agriculture and waste, followed by fuel exploitation, while other sectors are comparatively minor. It is also worth noting that wetland-like CH_4 emissions from rice paddies are categorized under the anthropogenic agricultural sector in EDGAR and are therefore included in our prior emissions. The inventory data used in this study, EDGAR, does not include natural wetland methane emissions and it is reported that annual CH_4 emission from natural wetlands in Korea is about 0.001 – 0.01 Tg CH_4 (Zhang et al., 2025). This is less than 0.5% of the national total anthropogenic CH_4 emissions.

Annual spatial distributions of CO_2 and CH_4 emissions across the domain are shown in Fig. 2. To consider temporal variability in CO_2 emissions by human activities and disaggregate to hourly emissions, we apply the monthly and diel scaling factors reported by the EDGAR and the gridded Temporal Improvements for Modelling Emissions by Scaling (TIMES) factors, respectively. These account for building heating/cooling usage patterns, traffic volume fluctuations, sectoral contributions (residential, commercial, transportation emission), and weekday-weekend differences at 0.25° × 0.25° resolutions (Nassar et al., 2013). Over ocean grid cells, EDGAR emissions are near zero except along major shipping lanes (if included in the selected EDGAR sectors). For CH_4 anthropogenic emissions, no diurnal TIMES disaggregation is applied; temporal variation is retained at the monthly level.

The spatial distribution of annual anthropogenic CO_2 and CH_4 emissions highlights the main source regions within the model domain (Fig. 2b and 2c). Strong CO_2 emissions in the Seoul Metropolitan Area (SMA) reflect aggregated contributions from power plants, traffic, and building emissions in the urban area. Industrial processes and power generation dominate emissions in the MWI and south and southeastern coast industrial corridors (SCI and SEI) over the Korean Peninsula (Fig. S3). CH_4 sources are generally coincident with strong CO_2 emission regions due to waste management in highly populated area but exhibit more spatially confined peaks with hotspots over the high-density urban area (SMA) (wastewater and landfills) and central livestock area (CLA) (enteric fermentation and manure management) (Fig. S4).

5.2 Biomass burning emissions

Biomass burning emissions of CO_2 and CH_4 are taken from the Fire Inventory from the National Center for Atmospheric Research (NCAR) (FINN version 2.5). This dataset estimates biomass burning emissions using burned-area calculations, year-specific land cover and vegetation datasets, fuel loading and emission factors, and the use of multiple fire-detection satellites, such as MODerate resolution Imaging Spectroradiometer (MODIS) and Visible Infrared Imaging Radiometer Suite (VIIRS) (Schroeder et al., 2014). FINN provides emissions at 1 km spatial resolution and daily temporal resolution (Wiedinmyer et al., 2011; Callewaert et al., 2022; Wiedinmyer et al., 2023). The NCAR fire-emission preprocessing tool is used to subset the inventory over the modeling domain, regrid it to the model grid, and temporally disaggregate it to hourly emissions for WRF-Chem GHG simulations. Biomass burning emissions show strong spatial and seasonal variability in our domain (Fig. S5 for CO_2 and Fig. S6 for CH_4). Seasonal enhancements are primarily observed in spring (March–May), possibly related to agricultural residue burning and land-clearing practices. The total contribution of biomass burning emissions over the Korean Peninsula is negligible compared with anthropogenic emissions (< 0.1%) during the study period (2020).

5.3 Ocean CO_2 exchanges

Air-sea CO_2 exchange is obtained from the latest SeaFlux Ocean Carbon Dioxide Flux product (v2023.02) (Roobaert et al., 2018; Roobaert et al., 2019; Fay et al., 2021). This dataset combines five meteorological reanalysis data with six ocean surface CO_2 datasets, making a total of 30 combinations of the data products. These data provide monthly ocean CO_2 fluxes on a 1°×1° grid for 1990-2022. For this study, ensemble-mean monthly exchanges are used for oceanic CO_2 fluxes and prescribed as hourly fluxes (i.e., held constant throughout each month without sub-monthly or diurnal variability). Monthly distribution of oceanic CO_2 exchanges over East Asia shows that the Yellow Sea and nearby shelves exhibit seasonal reversals in oceanic CO_2 fluxes (i.e., net uptake during winter and spring and a source in summer) (Fig. S7) (Gregor and Fay, 2021). In contrast, the deeper East Sea acts as a persistent CO_2 sink. Although these patterns reflect known contrasts between shallow shelves and deep basins, the oceanic flux magnitude in our domain configuration is small relative to the dominant anthropogenic and terrestrial biogenic CO_2 sources and sinks.

5.4 VPRM-based estimation of terrestrial ecosystem fluxes

Terrestrial ecosystem carbon fluxes are estimated with the Vegetation Photosynthesis and Respiration Model (VPRM) coupled with WRF-Chem (Ahmadov et al., 2007; Mahadevan et al., 2008). VPRM simulates net ecosystem exchange (NEE) of CO_2 using meteorological drivers and satellite-derived surface indices, specifically the Enhanced Vegetation Index (EVI) and Land Surface Water Index (LSWI) from MODIS Terra surface reflectance 8-Day 500m product (MOD09A1). During model integration, VPRM computes Gross Primary Production (GPP) and ecosystem respiration (RES) and derives NEE as RES-

GPP (negative NEE indicates net uptake in our sign convention) for eight land-cover categories using EVI, LSWI, 2 m air temperature, and Photosynthetically Active Radiation (PAR) derived from downward shortwave radiation simulated by WRF-Chem. Vegetation inputs (plant functional type, vegetation cover fraction, EVI, and LSWI) are derived from the 1-km SYNMAP global land cover data and MOD09A1 and are preprocessed using the VPRM preprocessor (Jung et al., 2006). VPRM-derived terrestrial CO_2 fluxes are sensitive to parameters linking EVI, LSWI, temperature, and radiation to GPP and RES (Hilton et al., 2013; Dayalu et al., 2018; Li et al., 2020). Because each vegetation type has distinct responses to environmental drivers, parameter calibration is critical to reduce NEE biases across Plant Functional Types (PFTs, i.e., vegetation categories). In this study, we adopt a single parameter set (λ: maximum light use efficiency, PAR_0: half-saturation value of PAR, α: temperature sensitivity of respiration, and β: basal respiration rate) applied uniformly across PFTs (vegetation categories) reported by Li et al. (2020), which has been validated for East Asian land-cover conditions to better capture seasonal and ecological variations across the Korean Peninsula.

Terrestrial biogenic CO_2 fluxes from the VPRM show strong seasonality driven by photosynthetic activity and temperature-dependent respiration (Fig. 3a). Croplands, deciduous, and mixed forests dominate in the model domain and contribute most to net carbon uptake during the growing summer season. Savanna and shrubland play minor roles in total uptake due to their limited areal extent. Monthly NEE shows clear net carbon uptake (negative values) in the summer growing season (May to September) with the strongest uptake (i.e., most negative NEE) in July when GPP exceeds RES, with relatively larger uncertainties in biogenic CO_2 fluxes. The monthly mean diurnal cycles of GPP, RES, and NEE further highlight that daytime GPP peaks in summer is mainly driven by higher incoming shortwave radiation and by more gradual, temperature-driven RES associated with the seasonal progression of the summer monsoon (Fig. S8) (Hong and Kim, 2011). For 2020, the integrated NEE over South Korea is −43 Mt CO_2 (5% of national anthropogenic GHG emissions) and broadly consistent with the national inventory estimate of the Land Use, Land Use Change and Forestry (LULUCF) sink (−39 Mt CO_2; Ministry of Environment, Republic of Korea, 2025), indicating that the VPRM biogenic fluxes reasonably represent the terrestrial carbon sink in this system.

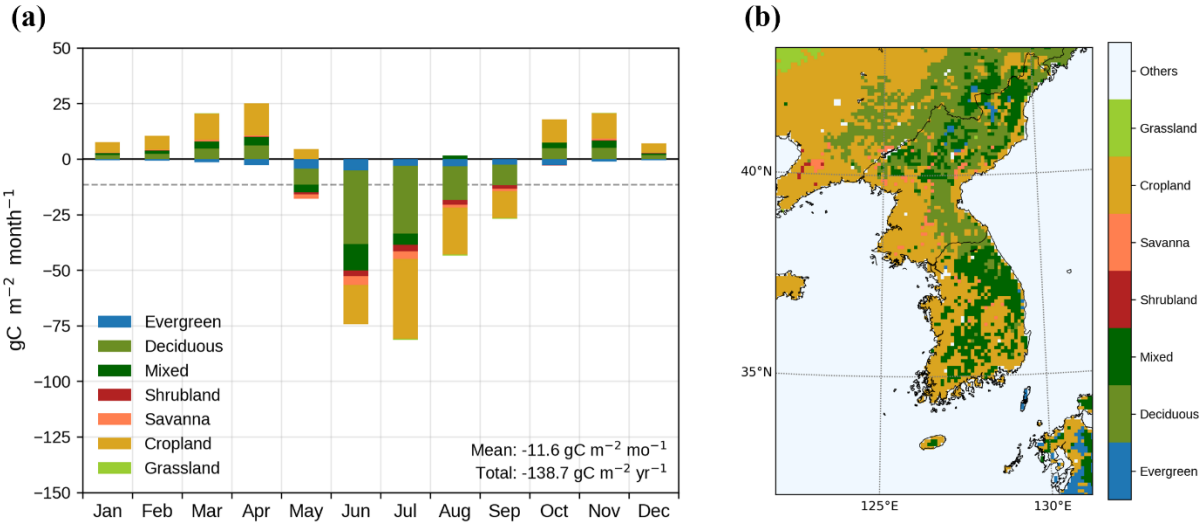

Figure 3. (a) Monthly net ecosystem exchange (NEE) contributions by vegetation class over the model domain in 2020. Bars show class totals (g C m⁻² month⁻¹), computed as spatial averages over grid cells of the corresponding vegetation type; negative values indicate net carbon uptake. (b) Spatial distribution of dominant vegetation classes used in WRF-Chem/VPRM; each grid cell is assigned the class with the largest vegetation fraction. Colors are consistent across panels.

6 Evaluation of the top-down estimates for 2020 case study

We now present a real-data demonstration to assess how the same cycling and analysis configuration performs under real observational constraints and inevitable model-data inconsistencies. We evaluated inversion results for 2020 using the WRF-Chem/DART system with full DA, in which both meteorological and GHG observations were assimilated. Each monthly run was initiated at 00 UTC on the last day of the preceding month, followed by a 24-hour spin-up prior to the start of assimilation.

6.1 GHG concentrations at ground stations

Monthly distributions of prior, posterior, and observed CO_2 and CH_4 concentrations at the three WMO/GAW surface stations are summarized with box plots for comparison of seasonal variability and site-to-site statistics (Fig. 4 and Table 1). Prior CO_2 concentrations overestimate the *in situ* observations at the AMY by about 12 ppm but underestimate at the remote stations (ULD and GSN) by 2-3 ppm. Prior CH_4 concentrations underestimate at all stations with annual mean biases of -52 to -88 ppb and particularly large discrepancies during the summer season. These biases are consistent with the expected influence of uncertainties in the prescribed EGG4 boundary fields. The top-down estimates of GHG concentrations show markedly improved agreement with observations relative to the prior, indicating the practical effectiveness of the EAKF system in reducing concentration-space mismatches. At the observation locations, the posterior estimates generally fall between the prior

and the observations. Across all sites and both species, posterior estimates consistently reduce MBE (mean bias error) and RMSE (root mean square error) (Table 1). Mean bias of posterior surface CO_2 and CH_4 concentrations are in the ranges of 1-2 ppm and 20-30 ppb, respectively. The drivers of these improvements vary by site. The largest error reduction for CO_2 occurs at AMY (10.9 ppm), consistent with correction of a substantial prior positive concentration bias associated with nearby industrial sources and regional transport. In contrast, the largest improvement for CH_4 occurs at GSN (57 ppb), driven principally by the correction of the background bias and compensation for the latitudinal CH_4 gradient inherited from the CAMS EGG4 boundary conditions. Note that the DA system does not directly modify OH fields; rather, it adjusts CH_4 concentrations to match observations. Error reductions are most pronounced in summer, consistent with corrections to low-biased boundary inflow for CH_4 and to underrepresented seasonal regional fluxes (e.g., anthropogenic and biogeochemical contributions) when seasonal gradients are largest.

Notable differences are evident in the skewness of the monthly distributions of observed CO_2 and CH_4 concentrations across the sites. At AMY, both prior and posterior CO_2 and CH_4 exhibit strong positive skewness and high variability (elongated upper whiskers in Fig. 4a and 4d), depending on wind around nearby large point sources (i.e., power and industrial plants in the MWI). In contrast, GSN and ULD show more symmetric, compact distributions, suggesting weaker local source influence on these remote stations. All three stations exhibit a pronounced summertime dip in CH_4 concentration, especially in August. This feature is also evident in the EGG4 boundary fields used as lateral forcing (Fig. S11), suggesting that it primarily reflects large-scale seasonal background variability, potentially including enhanced summertime oxidative loss at hemispheric to continental scales, rather than regional chemical loss within the WRF-Chem domain.

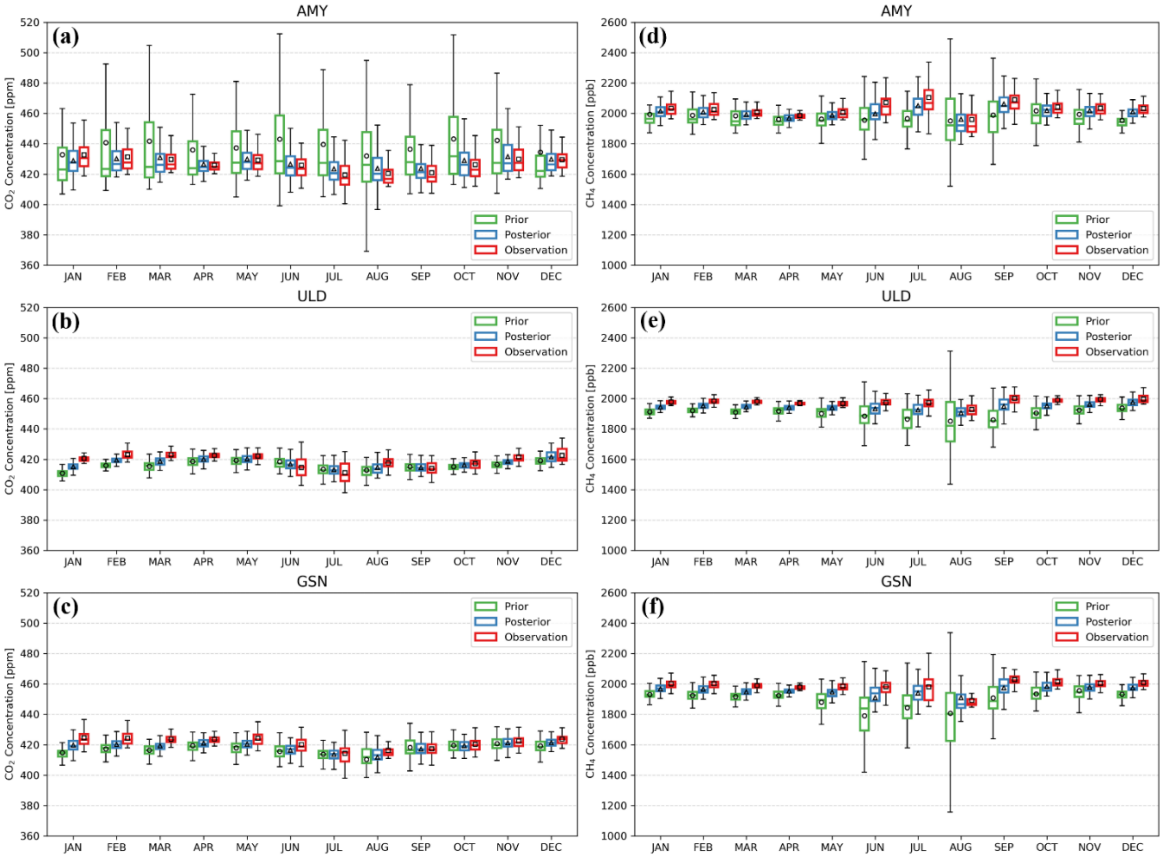

460 **Figure 4. Monthly boxplots of CO_2 (a–c) and CH_4 (d–f) concentrations at AMY (a,d), ULD (b,e), and GSN (c,f) in 2020. Prior (green), posterior (blue), and observations (red) are shown for each site. Boxes denote the interquartile range (25th–75th percentiles); horizontal lines indicate medians. Symbols denote means (prior: circle; posterior: triangle; observation: square).**

Table 1. Mean bias error (MBE) and root-mean-square error (RMSE) of the top-down estimates to the observations at AMY, ULD, and GSN in 2020. Statistics are computed from 6-hourly averages.

Station name	Latitude	Longitude	GHG variable	MBE	RMSE
AMY	36.53°N	126.32°E	Prior CO_2	12.1 ppm	35.2 ppm
			Posterior CO_2	1.2 ppm	13.9 ppm
			Prior CH_4	-52 ppb	163 ppb
			Posterior CH_4	-23 ppb	111 ppb
ULD	37.48°N	130.90°E	Prior CO_2	-2.4 ppm	7.7 ppm
			Posterior CO_2	-1.2 ppm	5.4 ppm
			Prior CH_4	-72 ppb	124 ppb
			Posterior CH_4	-30 ppb	60 ppb
GSN	33.29°N	126.16°E	Prior CO_2	-3.4 ppm	10.0 ppm
			Posterior CO_2	-2.3 ppm	7.4 ppm
			Prior CH_4	-88 ppb	179 ppb
			Posterior CH_4	-31 ppb	109 ppb

6.2 Validation against aircraft observations

To independently evaluate the performance of the inversion system, posterior CO_2 and CH_4 concentrations are compared with aircraft-based *in situ* observations collected over the Yellow Sea near the AMY station in 2020 using a Beechcraft King Air 350. The aircraft was equipped with a CRDS (G2401, Picarro Inc., USA) for measuring CO_2, CH_4, CO, and H_2O, at a sampling rate of 1.5 Hz. Sample air was dried upstream, and inlet ports were located near the front fuselage to minimize contamination. Typical operating altitudes reached 10 km with cruising speeds of 70–120 m s^{-1}, supporting both routine profiling and regional transport characterization. Ten vertical profile flights near the AMY were available in 2020 (not used in the data assimilation) (Fig. S9). After quality control, the profiles were aggregated into 1 km altitude bins (±500 m). Model fields were sampled along the flight track (time-matched and horizontally interpolated to the observation location) and averaged into the same altitude bins. For each bin, we computed mean observed concentrations and observational uncertainties (quadrature of sampling variability and reported measurement uncertainty) alongside the corresponding posterior values.

Figure 5 presents vertical profiles for CO_2 and CH_4 concentrations from both the inversion system and aircraft. Posterior CO_2 concentration is in good agreement with the observed profile with biases of 1-5 ppm even in the upper troposphere,

whereas the posterior CH_4 concentration profile shows a systematic negative bias of 40–50 ppb from the boundary layer to the mid-troposphere. We speculate that this persistent CH_4 bias likely reflects a combination of residual boundary condition bias in the prescribed CAMS EGG4 inflow mole fraction and under-represented coastal CH_4 sources in prior data over the Yellow Sea. A controlled boundary-condition experiment supports the plausibility of this interpretation: imposing a CH_4 background bias of known size produces the weakest near-station CH_4 recovery, with a much smaller CO_2 response, consistent with the species-specific signature seen in the aircraft comparison (Supplement Sect. S1.3, Fig. S17). We present this as a consistency check rather than a unique attribution. It does not exclude possible contributions from under-represented coastal or inland CH4 sources, residual transport error, or other boundary-condition uncertainties. The latter is consistent with the report that shallow shelves and coastal waters can be important CH_4 source regions (Lee et al., 2018; Weber et al., 2019). These results motivate further investigation of maritime CH_4 contributions in the regional prior/boundary treatment and highlight the value of additional observational constraints for improving CH_4 budgets over the Korean Peninsula.

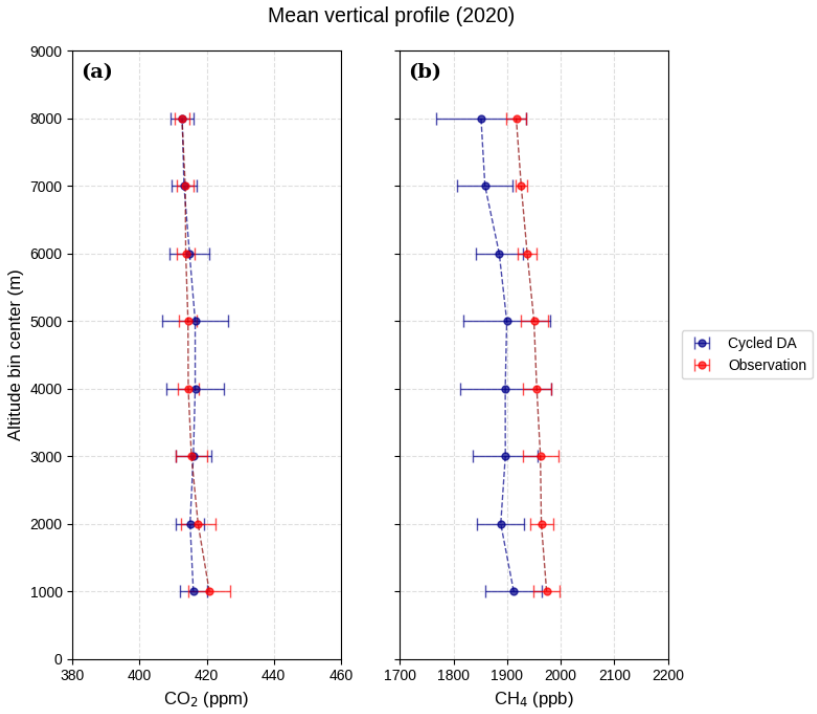

Figure 5. Mean vertical profiles of CO_2 and CH_4 from 10 CM-01 flights over South Korea in 2020. Profiles are aggregated into 1 km altitude bins (±500 m). Symbols and error bars show mean concentrations and associated uncertainties per bin: observations (red) and cycled DA (blue). Observation uncertainties combine measurement precision and sampling variability.

6.3 Uncertainty reduction in concentrations and fluxes

Figures 6 and 7 show the spatial distributions of ensemble spreads for CO_2 and CH_4 concentrations and the corresponding emission uncertainties, respectively, showing prior uncertainties (left panels) and uncertainty reductions after the DA (right panels). Unless noted, "uncertainty reduction" is defined as $(1-\sigma_{post}/\sigma_{prior}) \times 100$ % over grid cells where σ_{post} and σ_{prior} denote the posterior and prior ensemble spread, respectively. Domain-averaged concentration uncertainty over land decreases by 25-35 % for CO_2 and about 20 % for CH_4, with local reductions up to 50 % near the observation sites. Prior uncertainties in both concentrations and anthropogenic fluxes are elevated over strong source regions in SMA, large-scale power plants along the MWI, and the southeastern industrial areas (SCI and SEI) for CO_2. Elevated uncertainties for CH_4 are observed in landfills around the SMA, and in rice cultivation areas, as well as at livestock farms around CLA (compare Fig. 2 with Fig. 6 and 7). Posterior uncertainties in GHG concentrations decrease substantially within an influence radius of about 90 km (e-folding distance) from all the stations. CH_4 uncertainty reduction reaches up to 40 % around the station and has a larger relative decrease than CO_2. This is consistent with the negative bias in CH_4 concentration discussed above. We also note that uncertainty reductions over North Korea and China arise from weak cross-covariances at the range limit; these transboundary updates are not quantitatively interpreted in this study.

The spatial patterns of prior flux uncertainties closely resemble those for concentrations. Overall uncertainties for CO_2 emission decrease by about 7 % after the DA. CO_2 emission uncertainties decrease sharply within the influence radius of the AMY station along the western coasts, particularly for CO_2, where strong anthropogenic GHG sources are located (Fig. 7). Smaller reductions around ULD/GSN (< 5 %) reflect distance from major southeastern sources and prevailing winds. CH_4 emission uncertainties show a similar pattern with that of CO_2, except that the error reduction is relatively smaller than that of CO_2. Posterior flux uncertainty around AMY shows a relatively smaller reduction in CH_4 compared to CO_2, primarily because major CH_4 sources are located more easterly than those of CO_2. These patterns suggest qualitative priorities for future network expansion (e.g., enhanced CO_2 coverage in the southeastern industrial corridor and CH_4 coverage over central inland hotspots), while noting that a formal network optimization is beyond the scope of this paper. Because the maps are annual means, transient spatial structures at individual cycles are smoothed out; therefore, Figs. 6–9 should be interpreted as persistent features rather than cycle-to-cycle variability, with the strength of sub-national gradients remaining dependent on observational coverage.

The supplementary OSSE provides an idealized reference for this information-content limitation. Under perfect-model assumptions with a large prescribed prior-emission perturbation, the dense-network experiment (Figs S20–S22) shows stronger national-scale CO_2 emission recovery than the corresponding three-site experiment, whereas the three-site case exhibits much weaker recovery under otherwise matched filter settings. This contrast indicates that the modest domain-mean flux-uncertainty reduction in the 2020 real-data case is consistent with limited observational information content, while also depending on the prescribed error statistics, localization, and prior-emission uncertainty. The companion error-source matrix supports this coverage interpretation: under the prescribed perturbations, transport-model, boundary-condition, and observation-error changes produce bounded changes in domain-mean recovery, and degrading observation precision has a limited effect on the

domain-mean recovery under the tested configuration (Table S2). These results suggest that, for the present three-station setup, observational coverage is a dominant limitation on domain-wide recovery. Both the error-source matrix and the dense-network experiment are idealized diagnostics, not evidence of real-world flux accuracy or grid-scale resolvability.

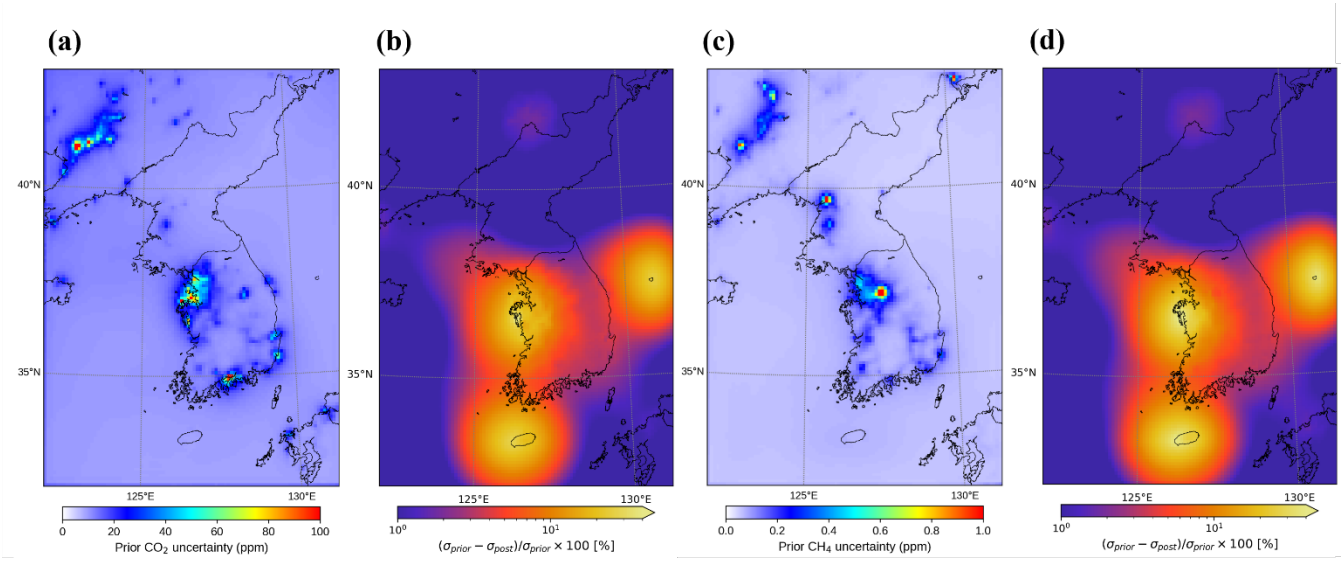

Figure 6. Annual prior concentration uncertainty (ensemble spread) (a,c) and its reduction after assimilation (b,d) for CO_2 (a,b) and CH_4 (c,d) in 2020.

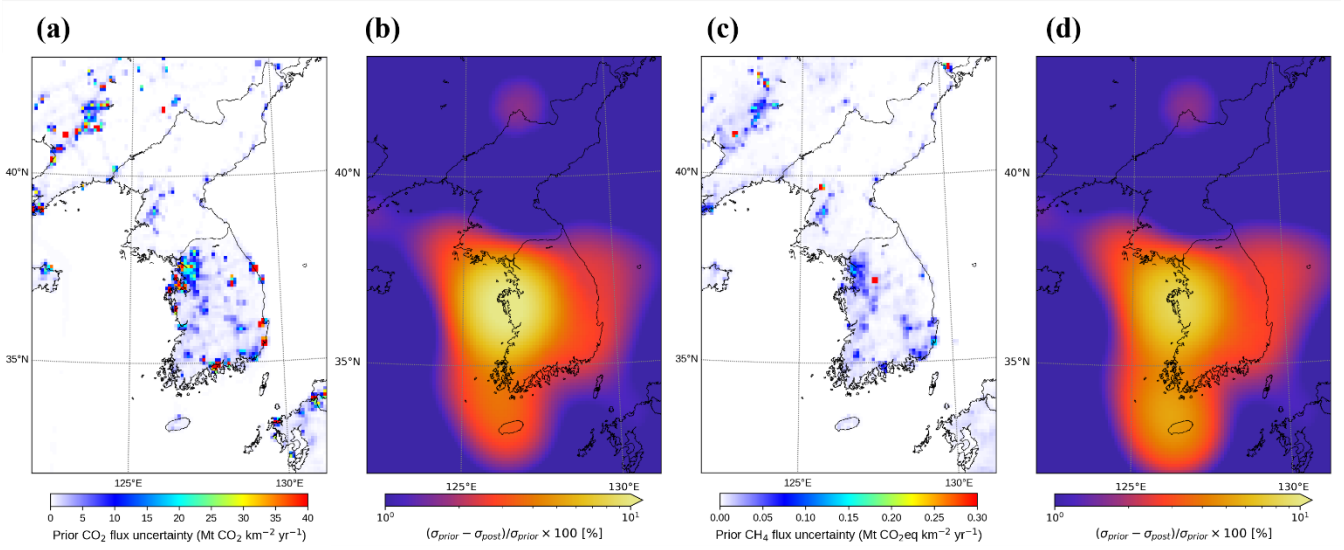

Figure 7. Annual prior flux uncertainty (a and c) and flux-uncertainty reduction (b and d) for CO_2 (a and b) and CH_4 (c and d) in 2020. Note that ocean-grid uncertainties are non-zero but appear small on the plotted scale because the prior spread is prescribed as a fractional perturbation and absolute oceanic flux magnitudes are much smaller than terrestrial sources.

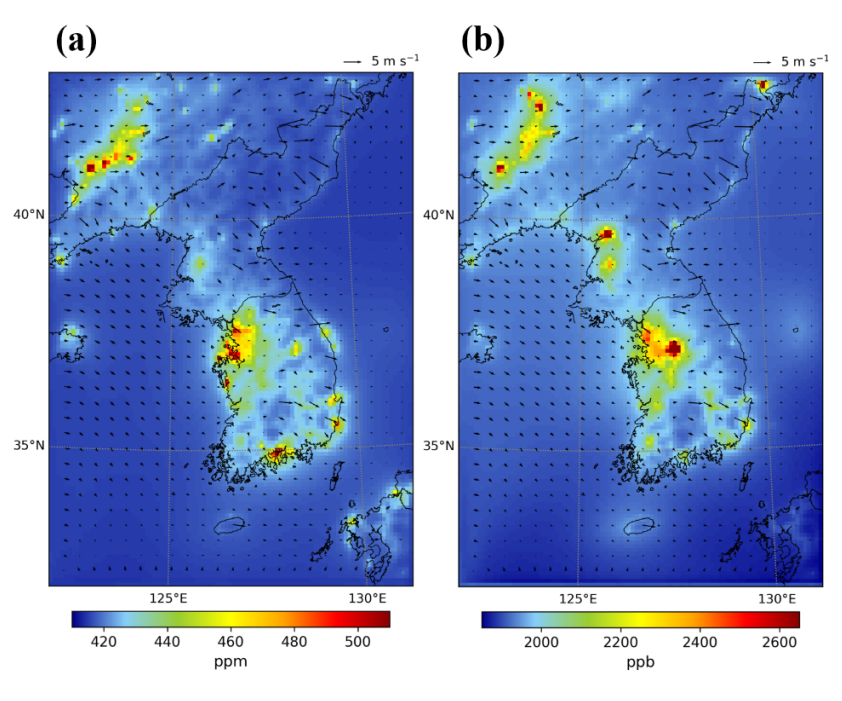

Figure 8. Annual mean surface posterior concentrations of CO_2 (a) and CH_4 (b) over the Korean Peninsula in 2020 from the WRF-Chem/DART inversion system. Wind vectors at 10 m illustrate prevailing flow conditions that shape annual concentration gradients.

545

6.4 Posterior fluxes and concentrations of CO_2 and CH_4

Figure 8 shows the spatial distribution of CO_2 and CH_4 concentrations from the inversion system. Posterior GHG concentrations capture large-scale gradients and regional enhancements induced by both long-range transport and upwind source regions. Elevated concentrations are clearly identified over key heavy industry and dense urban zones, specifically
550 along the SMA, the west coast, and the southern industrial corridor (MWI, SCI, and SEI; Fig. 2b) for CO_2. In contrast, enhanced CH_4 concentrations are more closely associated with agricultural and waste-related source regions, including central–western Korea and the CLA region (Fig. 2c). When viewed alongside CAMS EGG4, both fields exhibit the broad synoptic structures, including persistent enhancements over the western Korean Peninsula and eastern China and the seasonal cycle of winter accumulation and summer dilution (Figs. S10–S13). This comparison is not used as an emission benchmark, because EGG4
555 does not solve for regional emissions in the same sense as the present inversion system; rather, it is used to illustrate differences in concentration-field representation between the coarse global boundary product and the high-resolution regional posterior. The structural differences between the two products primarily reflect differences in resolution: while EGG4 depicts spatially smoother concentration fields characteristic of its 0.75° global resolution, the 9-km posterior estimates represent sharper concentration gradients and more distinct source-region signatures over the SMA and MWI (Figs. 8 and S14a). Similarly,

elevated CH_4 concentrations over the CLA are represented as more localized features in the posterior, whereas these appear as broader, more diffuse patterns in the global product (Fig. S14b). These features are consistent with previous satellite-based studies over Korea that documented fine-scale urban–industrial heterogeneity in CO_2 and CH_4 (Shim et al., 2019; Moon et al., 2024). The 9-km framework resolution is selected with future satellite-assimilation applications in view (e.g., TROPOMI CH_4 at ~7 km footprint), where sub-grid representation error directly affects the forward operator. The present three-station *in situ* configuration does not by itself demonstrate grid-scale emission constraints at this resolution; however, retaining the 9-km transport framework facilitates future satellite-assimilation applications, provided that appropriate column observation operators, bias treatment, and representativeness-error specifications are implemented.

Figure 9 summarizes the posterior anthropogenic flux fields and the spatial distribution of flux adjustments (posterior minus prior). The overall spatial patterns of posterior CO_2 and CH_4 emissions remain similar to the priors, retaining the major hotspots over the Korean Peninsula (Fig. 2b and 2c), as expected, given the current observing network and the use of covariance localization. Spatially-varying posterior adjustments are nonetheless produced to reduce concentration innovations at the observation sites. With the current observation configuration, these adjustments are best interpreted as regionally coherent corrections within the localization-supported influence region, while finer-scale structure remains strongly constrained by the prior and the assumed error statistics. Negative increments in CO_2 emissions are concentrated in densely populated and traffic-heavy regions (SMA and MWI) and positive increments are observed along the east coast and in the southeastern industrial corridor (i.e., SCI and SEI) (Fig. 9b). These patterns are broadly consistent with the signs of the station-based concentration biases (Table 1) and suggest that the positive bias at AMY tends to project onto nearby western source regions as flux reductions, whereas the negative biases at GSN and ULD can contribute to increased fluxes in the southern and eastern industrial regions through localized concentration–flux covariances. This behavior may also reflect sector-dependent structural uncertainties in the priors, given the strong contribution of heavy industry (steel, petrochemical, shipbuilding, and vehicle manufacturing) in SCI and SEI, relative to the more mixed urban/energy source in SMA/MWI. Positive increments for CH_4 emission are widespread across inland source regions associated with rice paddy, livestock facilities, landfills, and power-industry (Fig. 9d). Given the persistent negative CH_4 bias in the independent aircraft profiles (Section 6.2), we interpret these increases with caution because of the possibility for compensation for low-biased prescribed boundary mole fractions. At the same time, the spatial correspondence with known inland hotspots suggests that missing or underestimated sources in the prior may also contribute. The controlled OSSE matrix provides a scale for interpreting these sensitivities under prescribed conditions: transport-model, boundary-condition, and observation-error perturbations change the recovered domain emission by only a few percentage points of the prior inventory in the tested configuration, while the localization sweep produces somewhat larger changes (Table S2, Supplement Sect. S1.2–S1.3). These values should be interpreted as controlled diagnostic responses, not as universal bounds on real-world error. Further work with alternative boundary products and expanded observational constraints (e.g., additional in situ and upper-air measurements) is needed to extend this across the multiple sectors, times, and regions of a real application.

Figure 10 compares national-total anthropogenic CO_2 and CH_4 emissions for South Korea in 2020 from the posterior with multiple bottom-up inventories. For CO_2, the comparison encompasses Open-source Data Inventory for Anthropogenic CO_2 (ODIAC) (Oda et al., 2018), the Fossil Fuel Data Assimilation System (FFDAS) (Rayner et al., 2010), the Gridded Daily Fossil CO_2 Emissions Dataset (GRACED) (Dou et al., 2023), EDGAR, and the national total anthropogenic emissions (excluding the LULUCF sector) as reported in the Biennial Transparency Report of the Republic of Korea (ROK-BTR, hereafter). Because these products differ substantially in scope and construction (e.g., fossil-fuel-only versus IPCC-sector totals), proxy choice, point-source treatment, spatial disaggregation, native resolution, and sector attribution, we interpret the comparison as a consistency check under a harmonized scope (anthropogenic CO_2 excluding LULUCF) rather than as a validation target (Hutchins et al., 2017). Under the harmonized scope and spatial aggregation used here, EDGAR's national-total anthropogenic CO_2 is most consistent with the ROK-BTR estimate among the bottom-up datasets considered. EDGAR is the closest to ROK-BTR (4 % higher), whereas FFDAS, GRACED, and ODIAC show larger deviations, ranging from about -31 % to +10 %. In 2020, our posterior CO_2 total is broadly consistent with ROK-BTR at the national scale (Fig. 10). In contrast, posterior CH_4 total shows weaker agreement with the available bottom-up estimates, consistent with the larger structural uncertainty in CH_4 source characterization and spatial allocation noted in previous studies (e.g., Moon et al., 2024).

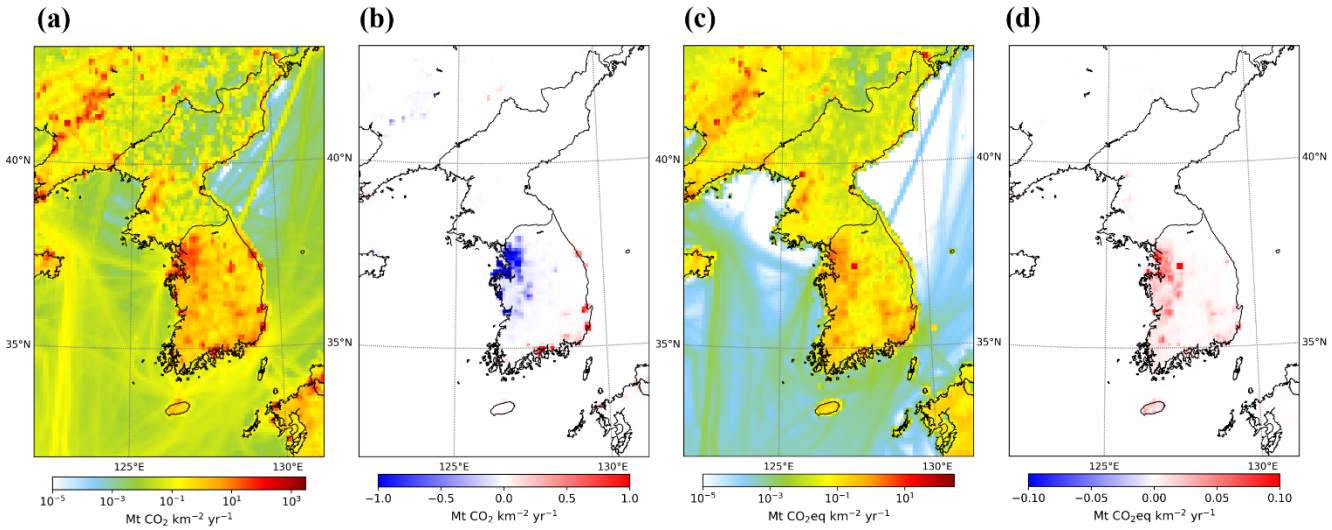

Figure 9. Annual-mean posterior surface fluxes (a and c) and assimilation increments (posterior minus prior) (b and d) for CO_2 (a and b) and CH_4 (c and d) from the WRF-Chem/DART system. Red (blue) shading indicates an increase (decrease) in the posterior relative to the prior.

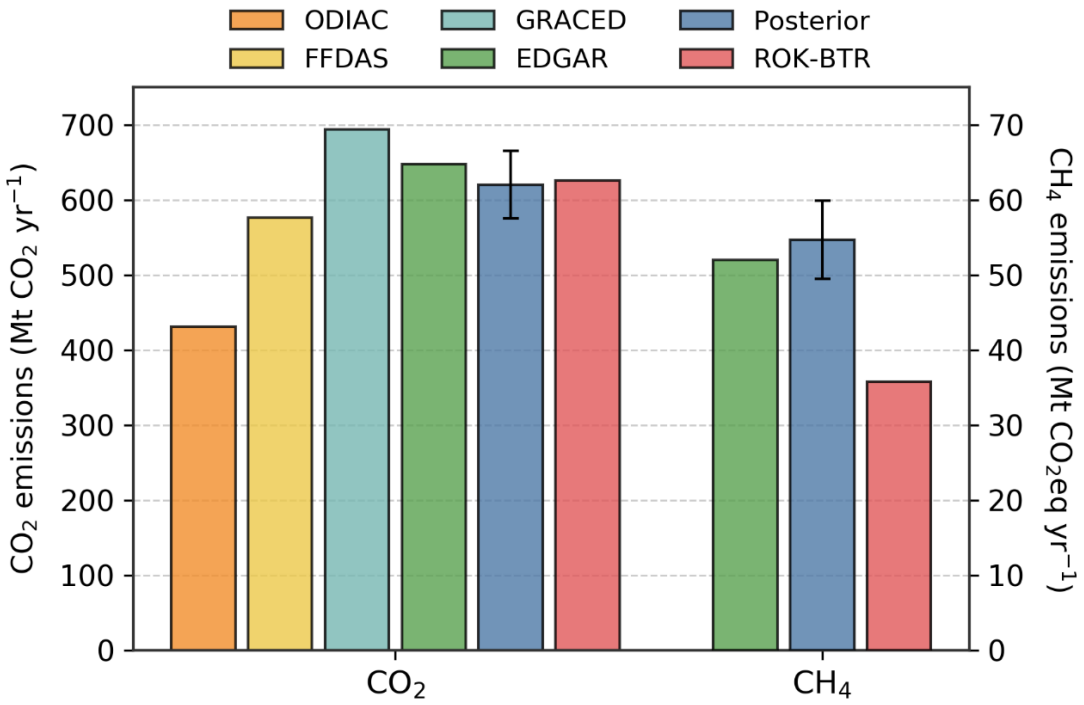

Figure 10. Annual total anthropogenic CO_2 and CH_4 emissions over South Korea in 2020 from multiple datasets. CO_2 comparisons include ODIAC, FFDAS, GRACED, EDGAR, ROK-BTR, and the posterior (six sources). CH_4 comparisons include EDGAR, ROK-BTR, and the posterior. Error bars denote posterior uncertainty. (FFDAS was scaled using the 2015–2020 gross emission growth rate from ROK-BTR because FFDAS is available only through 2015)

7 Summary and Conclusion

This study presents a high-resolution dual-species GHG (CO_2 and CH_4) inversion framework using the coupled WRF-Chem/DART system, which assimilates continuous high-precision *in situ* observations of GHG concentrations. The system provides transport-consistent and observation-constrained emission estimates and dynamically consistent temporal state updates through ensemble data assimilation. By updating both meteorological and tracer states within the cycling system, the framework maintains internally consistent transport–concentration relationships over complex terrain. The incorporation of continuous high-frequency *in situ* observations helps constrain near-surface gradients and the associated anthropogenic flux sensitivity.

This framework is designed to accommodate denser and more diverse observing systems (e.g., additional surface sites, tall towers, aircraft profiles, and satellite column retrievals) within the same data-assimilation framework; although extending to various types of observations may involve implementing the corresponding observation operators and specifying observation-error/representativeness settings (including bias treatment where applicable), together with network-dependent tuning (e.g., localization and observation error) as needed. A controlled OSSE matrix shows that, under prescribed transport-model, boundary-condition, and observation-error perturbations, the system produces bounded and interpretable emission responses

rather than unbounded or unstable corrections. The complementary dense-network known-truth experiment indicates that expanded observational coverage substantially strengthens domain-wide CO_2 emission recovery in an idealized setting, while the real-case diagnostics of ensemble size and inflation configuration support the current 20-member, adaptive-inflation setup as a practical configuration rather than a uniquely optimized one.

The cycling dual-state EAKF framework provides an integrated treatment of background errors and filter stability within a joint state–parameter assimilation system for GHG concentrations and emissions. Because meteorology and 3-D tracer fields are advanced and analyzed within the same model, background-error covariances are represented in a flow-dependent manner by the evolving ensemble. The DART configuration provides an explicit, principled inflation framework to maintain physically plausible ensemble spread and to mitigate ensemble collapse during repeated cycling, offering a systematic handle on under-dispersion arising from unresolved transport/model errors and finite-ensemble sampling. These capabilities come with trade-offs. Running an ensemble is computationally more expensive than footprint-based calculations, and posterior updates depend on the fidelity of the underlying meteorological and sub-grid physical parameterizations that govern transport and mixing.

In the 2020 real-data application, the system reduces mismatches with observed CO2 and CH4 at all high-precision sites and yields posterior uncertainty reduction in both concentrations and emissions. The posterior surface biases are reduced to approximately 1-2 ppm for CO_2 and 20-30 ppb for CH_4 across the WMO/GAW sites in 2020, indicating improved consistency with local observations under the cycling configuration relative to the prescribed CAMS EGG4 IC/BC forcing. The posterior national CO_2 total (620 ± 45 Mt yr^{-1}) is consistent with the ROK-BTR estimate (624 Mt yr^{-1}) at the national scale. The posterior CH_4 total (54.7 ± 5.2 Mt CO_2eq yr^{-1}), however, exceeds the ROK-BTR estimate (35.5 Mt CO_2eq yr^{-1}) by 19.2 Mt CO_2eq yr^{-1}, which may reflect a combination of underestimated agricultural and waste-sector sources, residual boundary-condition bias, and structural uncertainty in CH_4 source characterization and spatial allocation. Regional adjustments relative to the prior are observed over densely populated, industrial, and agricultural areas for both species. Posterior increments suggest that prior CO_2 emissions may be overestimated over the Seoul Metropolitan Area and portions of the western coastal region, whereas CH_4 emissions may be underestimated over inland agricultural hotspots; CH_4 adjustments should be interpreted with caution, given the potential sensitivity to boundary-condition biases and maritime source representation. These results illustrate the potential value of top-down constraints for national-scale consistency checks and for guiding sub-national inventory evaluation. The current three-station configuration provides the strongest constraints within station footprints and should therefore be interpreted as a first operationally relevant regional demonstration, not as a claim of grid-scale emission resolvability. Broader observing-system configurations, including additional surface stations, upper-air measurements, and satellite column retrievals with appropriate bias and representativeness-error treatment, remain the primary pathway for improving domain-wide emission constraints. To our knowledge, this study provides the first fully documented regional WRF-Chem/DART workflow for simultaneous CO_2 and CH_4 estimation within a cycling dual-state configuration at kilometer-scale resolution, combining in situ GHG assimilation with meteorological data assimilation. Overall, this high-resolution dual-species WRF-Chem/DART inversion framework leveraging surface heterogeneity-aware parameterizations provides a reproducible basis for spatially

explicit emission analyses that can support future policy applications, operational monitoring development, and MMRV-oriented evaluation at national and sub-national scales.

Code and Data availability

Model source code used in this study are archived on Zenodo under https://doi.org/10.5281/zenodo.16939122 (Kwon et al., 2025a). Preprocessed data, model output, and model configurations used in this study are archived on Zenodo under https://doi.org/10.5281/zenodo.16947463 (Kwon et al., 2025b). ERA5 is available after registration at https://doi.org/10.24381/cds.adbb2d47 (pressure levels) (Hersbach et al., 2023a) and https://doi.org/10.24381/cds.bd0915c6 (single level) (Hersbach et al., 2023b). CAMS EGG4 is available after registration at https://doi.org/10.24381/cda4ed31 (Copernicus Atmosphere Monitoring Service, 2021). PREPBUFR is available at https://doi.org/10.5065/Z83F-N512 (National Centers for Environmental Prediction, 2008). EDGARv8.0 is available at https://edgar.jrc.ec.europa.eu/dataset_ghg80 (Crippa et al., 2023). FFDAS is available at https://ffdas.rc.nau.edu/Data.html (Rayner et al., 2010). GRACED is available after registration at https://carbonmonitor-graced.com (Dou et al., 2023). ODIAC is available at https://doi.org/10.17595/20170411.001 (Oda et al., 2015). FINNv2.5 is available after registration at https://doi.org/10.5065/XNPA-AF09 (Wiedinmyer and Emmons, 2022). SeaFlux is available at https://doi.org/10.5281/zenodo.5482547 (Gregor and Fay, 2021). Annual budget of CO_2 and CH_4 emissions in South Korea is available under https://unfccc.int/documents/645637 (Biennial Transparency Report of Republic of Korea, 2025). EDGARv8.0, FFDAS, GRACED and the Republic of Korea's Biennial Transparency Report are also archived on Zenodo under https://doi.org/10.5281/zenodo.17402804 (Kwon et al., 2025c). Access to the repositories archived on Zenodo will be provided upon request to the corresponding author.

Author contributions

DK, BK, ES, AA, CS, DS, SK, SJ, and JH conceptualized and designed the study. DK, BK, JL, JK, ES, and AA contributed to the implementation and development of the forward and inverse modeling framework. DS, SL, SK, and SJ were responsible for the WMO/GAW KMA observation program and the aircraft-based measurement. DK and JA performed preprocessing and visualization of the VPRM inputs and outputs. DK and BK collected and processed the remaining input datasets, conducted the model simulations, and carried out the analysis and visualization. DK, BK, and JH prepared the original draft. All authors reviewed and edited the manuscript.

Competing interests

One of the authors is a member of the editorial board of Geoscientific Model Development.

Acknowledgements

We sincerely thank the editor, the editorial staff, and all the reviewers for their constructive comments and support, which significantly improved this paper. We received help from an AI tool for English improvement.

Financial support

This work was funded by the Korea Meteorological Administration Research and Development Program under Grant RS-2024-00404365.

References

Agustí-Panareda, A., Barré, J., Massart, S., Inness, A., Aben, I., Ades, M., Baier, B. C., Balsamo, G., Borsdorff, T., Bousserez, N., Boussetta, S., Buchwitz, M., Cantarello, L., Crevoisier, C., Engelen, R., Eskes, H., Flemming, J., Garrigues, S., Hasekamp, O., Huijnen, V., Jones, L., Kipling, Z., Langerock, B., McNorton, J., Meilhac, N., Noël, S., Parrington, M., Peuch, V.-H., Ramonet, M., Razinger, M., Reuter, M., Ribas, R., Suttie, M., Sweeney, C., Tarniewicz, J., and Wu, L.: Technical note: The CAMS greenhouse gas reanalysis from 2003 to 2020, Atmospheric Chemistry and Physics, 23, 3829–3859, https://doi.org/10.5194/acp-23-3829-2023, 2023.

Ahmadov, R., Gerbig, C., Kretschmer, R., Koerner, S., Neininger, B., Dolman, A. J., and Sarrat, C.: Mesoscale covariance of transport and CO2 fluxes: Evidence from observations and simulations using the WRF-VPRM coupled atmosphere-biosphere model, Journal of Geophysical Research: Atmospheres, 112, https://doi.org/10.1029/2007JD008552, 2007.

Anderson, J., Hoar, T., Raeder, K., Liu, H., Collins, N., Torn, R., and Avellano, A.: The Data Assimilation Research Testbed: A Community Facility, Bulletin of the American Meteorological Society, 90, 1283–1296, https://doi.org/10.1175/2009BAMS2618.1, 2009.

Anderson, J. L.: An Ensemble Adjustment Kalman Filter for Data Assimilation, Monthly Weather Review, 129, 2884–2903, https://doi.org/10.1175/1520-0493(2001)129<2884:AEAKFF>2.0.CO;2, 2001.

Anderson, J. L.: A Local Least Squares Framework for Ensemble Filtering, Monthly Weather Review, 131, 634–642, https://doi.org/10.1175/1520-0493(2003)131%253C0634:ALLSFF%253E2.0.CO;2, 2003.

Anderson, J. L.: Localization and Sampling Error Correction in Ensemble Kalman Filter Data Assimilation, Monthly Weather Review, 140, 2359–2371, https://doi.org/10.1175/MWR-D-11-00013.1, 2012.

Barker, D., Huang, X.-Y., Liu, Z., Auligné, T., Zhang, X., Rugg, S., Ajjaji, R., Bourgeois, A., Bray, J., Chen, Y., Demirtas, M., Guo, Y.-R., Henderson, T., Huang, W., Lin, H.-C., Michalakes, J., Rizvi, S., and Zhang, X.: The Weather Research and Forecasting Model's Community Variational/Ensemble Data Assimilation System: WRFDA, Bulletin of the American Meteorological Society, 93, 831–843, https://doi.org/10.1175/BAMS-D-11-00167.1, 2012.

Beck, V., Koch, T., Kretschmer, R., Marshall, J.and Ahmadov, R., Gerbig, C., Pillai, D., and Heimann, M.: The WRF Greenhouse Gas Model (WRF-GHG). Technical Report No. 25, Tech. rep., Max Planck Institute for Biogeochemistry, Jena, Germany, https://www.bgc-jena.mpg.de/5363366/tech_report25.pdf, 2012.

Biennial Transparency Report of Republic of Korea [data set], https://unfccc.int/documents/645637 (last access: 22 October 2025), 2025.

Bisht, J. S. H., Patra, P. K., Takigawa, M., Sekiya, T., Kanaya, Y., Saitoh, N., and Miyazaki, K.: Estimation of CH4 emission based on an advanced 4D-LETKF assimilation system, Geosci. Model Dev., 16, 1823–1838, https://doi.org/10.5194/gmd-16-1823-2023, 2023.

Brunner, D., Suter, I., Bernet, L., Constantin, L., Grange, S. K., Rubli, P., Li, J., Chen, J., Bigi, A., and Emmenegger, L.: Building-resolving simulations of anthropogenic and biospheric CO2 in the city of Zurich with GRAMM/GRAL, Atmospheric Chemistry and Physics, 25, 14387–14410, https://doi.org/10.5194/acp-25-14387-2025, 2025.

Bukosa, B., Mikaloff-Fletcher, S., Brailsford, G., Smale, D., Keller, E. D., Baisden, W. T., Kirschbaum, M. U. F., Giltrap, D. L., Liáng, L., Moore, S., Moss, R., Nichol, S., Turnbull, J., Geddes, A., Kennett, D., Hidy, D., Barcza, Z., Schipper, L. A., Wall, A. M., Nakaoka, S.-I., Mukai, H., and Brandon, A.: Inverse modelling of New Zealand's carbon dioxide balance estimates a larger than expected carbon sink, EGUsphere, 1–41, https://doi.org/10.5194/egusphere-2024-3866, 2025.

Bréon, F. M., Broquet, G., Puygrenier, V., Chevallier, F., Xueref-Remy, I., Ramonet, M., Dieudonné, E., Lopez, M., Schmidt, M., Perrussel, O., and Ciais, P.: An attempt at estimating Paris area CO_2 emissions from atmospheric concentration measurements, Atmospheric Chemistry and Physics, 15, 1707–1724, https://doi.org/10.5194/acp-15-1707-2015, 2015.

Byrne, B., Baker, D. F., Basu, S., Bertolacci, M., Bowman, K. W., Carroll, D., Chatterjee, A., Chevallier, F., Ciais, P., Cressie, N., Crisp, D., Crowell, S., Deng, F., Deng, Z., Deutscher, N. M., Dubey, M. K., Feng, S., García, O. E., Griffith, D. W. T., Herkommer, B., Hu, L., Jacobson, A. R., Janardanan, R., Jeong, S., Johnson, M. S., Jones, D. B. A., Kivi, R., Liu, J., Liu, Z., Maksyutov, S., Miller, J. B., Miller, S. M., Morino, I., Notholt, J., Oda, T., O'Dell, C. W., Oh, Y.-S., Ohyama, H., Patra, P. K., Peiro, H., Petri, C., Philip, S., Pollard, D. F., Poulter, B., Remaud, M., Schuh, A., Sha, M. K., Shiomi, K., Strong, K., Sweeney, C., Té, Y., Tian, H., Velazco, V. A., Vrekoussis, M., Warneke, T., Worden, J. R., Wunch, D., Yao, Y., Yun, J., Zammit-Mangion, A., and Zeng, N.: National CO_2 budgets (2015–2020) inferred from atmospheric CO_2 observations in support of the global stocktake, Earth System Science Data, 15, 963–1004, https://doi.org/10.5194/essd-15-963-2023, 2023.

Callewaert, S., Brioude, J., Langerock, B., Duflot, V., Fonteyn, D., Müller, J.-F., Metzger, J.-M., Hermans, C., Kumps, N., Ramonet, M., Lopez, M., Mahieu, E., and De Mazière, M.: Analysis of CO_2, CH_4, and CO surface and column concentrations observed at Réunion Island by assessing WRF-Chem simulations, Atmospheric Chemistry and Physics, 22, 7763–7792, https://doi.org/10.5194/acp-22-7763-2022, 2022.

Callewaert, S.: WRF-GHG user guide, Royal Belgian Institute for Space Aeronomy (BIRA-IASB), https://doi.org/10.18758/Q6RAPNEU, 2024.

Copernicus Atmosphere Monitoring Service: CAMS global greenhouse gas reanalysis (EGG4), CAMS Atmosphere Data Store (ADS) [data set], https://doi.org/10.24381/cda4ed31 (last access: 22 October 2025), 2021.

Crippa, M., Guizzardi D., Pagani F., Banja M., Muntean M., Schaaf E., Becker, W., Monforti-Ferrario F., Quadrelli, R., Risquez Martin, A., Taghavi-Moharamli, P., Grassi, G., Rossi, S., Brandao De Melo, J., Oom, D., Branco, A., San-Miguel, J., Vignati, E.: EDGAR v8.0 Greenhouse Gas Emissions, European Commission, Joint Research Centre (JRC) [data set] https://doi.org/10.2905/b54d8149-2864-4fb9-96b9-5fd3a020c224 (last access: 22 October 2025), 2023

Crippa, M., Guizzardi, D., Pagani, F., Schiavina, M., Melchiorri, M., Pisoni, E., Graziosi, F., Muntean, M., Maes, J., Dijkstra, L., Van Damme, M., Clarisse, L., and Coheur, P.: Insights into the spatial distribution of global, national, and subnational

greenhouse gas emissions in the Emissions Database for Global Atmospheric Research (EDGAR v8.0), Earth System Science Data, 16, 2811–2830, https://doi.org/10.5194/essd-16-2811-2024, 2024.

Custódio, D., Borrego, C., and Relvas, H.: Worldwide evaluation of CAMS-EGG4 CO_2 data re-analysis at the surface level, Toxics, 10, 331, https://doi.org/10.3390/toxics10060331, 2022.

Dayalu, A., Munger, J. W., Wofsy, S. C., Wang, Y., Nehrkorn, T., Zhao, Y., McElroy, M. B., Nielsen, C. P., and Luus, K.: Assessing biotic contributions to CO2 fluxes in northern China using the Vegetation, Photosynthesis and Respiration Model (VPRM-CHINA) and observations from 2005 to 2009, Biogeosciences, 15, 6713–6729, https://doi.org/10.5194/bg-15-6713-2018, 2018.

Dekker, I. N., Houweling, S., Aben, I., Röckmann, T., Krol, M., Martínez-Alonso, S., Deeter, M. N., and Worden, H. M.: Quantification of CO emissions from the city of Madrid using MOPITT satellite retrievals and WRF simulations, Atmospheric Chemistry and Physics, 17, 14675–14694, https://doi.org/10.5194/acp-17-14675-2017, 2017.

Deng, Z., Ciais, P., Tzompa-Sosa, Z. A., Saunois, M., Qiu, C., Tan, C., Sun, T., Ke, P., Cui, Y., Tanaka, K., Lin, X., Thompson, R. L., Tian, H., Yao, Y., Huang, Y., Lauerwald, R., Jain, A. K., Xu, X., Bastos, A., Sitch, S., Palmer, P. I., Lauvaux, T., d'Aspremont, A., Giron, C., Benoit, A., Poulter, B., Chang, J., Petrescu, A. M. R., Davis, S. J., Liu, Z., Grassi, G., Albergel, C., Tubiello, F. N., Perugini, L., Peters, W., and Chevallier, F.: Comparing national greenhouse gas budgets reported in UNFCCC inventories against atmospheric inversions, Earth System Science Data, 14, 1639–1675, https://doi.org/10.5194/essd-14-1639-2022, 2022.

Denison, S., Forster, P. M., and Smith, C. J.: Guidance on emissions metrics for nationally determined contributions under the Paris Agreement, Environ. Res. Lett., 14, 124002, https://doi.org/10.1088/1748-9326/ab4df4, 2019.

Dou, X., Hong, J., Ciais, P., Chevallier, F., Yan, F., Yu, Y., Hu, Y., Huo, D., Sun, Y., Wang, Y., Davis, S. J., Crippa, M., Janssens-Maenhout, G., Guizzardi, D., Solazzo, E., Lin, X., Song, X., Zhu, B., Cui, D., Ke, P., Wang, H., Zhou, W., Huang, X., Deng, Z., and Liu, Z.: Near-real-time global gridded daily CO_2 emissions 2021, Sci Data, 10, 69, https://doi.org/10.1038/s41597-023-01963-0, 2023.

Elguindi, N., Granier, C., Stavrakou, T., Darras, S., Bauwens, M., Cao, H., Chen, C., Denier Van Der Gon, H. A. C., Dubovik, O., Fu, T. M., Henze, D. K., Jiang, Z., Keita, S., Kuenen, J. J. P., Kurokawa, J., Liousse, C., Miyazaki, K., Müller, J.-F., Qu, Z., Solmon, F., and Zheng, B.: Intercomparison of Magnitudes and Trends in Anthropogenic Surface Emissions From Bottom-Up Inventories, Top-Down Estimates, and Emission Scenarios, Earth's Future, 8, e2020EF001520, https://doi.org/10.1029/2020EF001520, 2020.Enting, I. G.: Inverse Problems in Atmospheric Constituent Transport, Cambridge University Press, Cambridge, https://doi.org/10.1017/CBO9780511535741, 2002.

Fay, A. R., Gregor, L., Landschützer, P., McKinley, G. A., Gruber, N., Gehlen, M., Iida, Y., Laruelle, G. G., Rödenbeck, C., Roobaert, A., and Zeng, J.: SeaFlux: harmonization of air–sea CO_2 fluxes from surface pCO_2 data products using a standardized approach, Earth System Science Data, 13, 4693–4710, https://doi.org/10.5194/essd-13-4693-2021, 2021.

Friedlingstein, P., O'Sullivan, M., Jones, M. W., Andrew, R. M., Hauck, J., Landschützer, P., Le Quéré, C., Li, H., Luijkx, I. T., Olsen, A., Peters, G. P., Peters, W., Pongratz, J., Schwingshackl, C., Sitch, S., Canadell, J. G., Ciais, P., Jackson, R. B.,

Alin, S. R., Arneth, A., Arora, V., Bates, N. R., Becker, M., Bellouin, N., Berghoff, C. F., Bittig, H. C., Bopp, L., Cadule, P., Campbell, K., Chamberlain, M. A., Chandra, N., Chevallier, F., Chini, L. P., Colligan, T., Decayeux, J., Djeutchouang, L. M., Dou, X., Duran Rojas, C., Enyo, K., Evans, W., Fay, A. R., Feely, R. A., Ford, D. J., Foster, A., Gasser, T., Gehlen, M., Gkritzalis, T., Grassi, G., Gregor, L., Gruber, N., Gürses, Ö., Harris, I., Hefner, M., Heinke, J., Hurtt, G. C., Iida, Y., Ilyina, T., Jacobson, A. R., Jain, A. K., Jarníková, T., Jersild, A., Jiang, F., Jin, Z., Kato, E., Keeling, R. F., Klein Goldewijk, K., Knauer, J., Korsbakken, J. I., Lan, X., Lauvset, S. K., Lefèvre, N., Liu, Z., Liu, J., Ma, L., Maksyutov, S., Marland, G., Mayot, N., McGuire, P. C., Metzl, N., Monacci, N. M., Morgan, E. J., Nakaoka, S.-I., Neill, C., Niwa, Y., Nützel, T., Olivier, L., Ono, T., Palmer, P. I., Pierrot, D., Qin, Z., Resplandy, L., Roobaert, A., Rosan, T. M., Rödenbeck, C., Schwinger, J., Smallman, T. L., Smith, S. M., Sospedra-Alfonso, R., Steinhoff, T., Sun, Q., Sutton, A. J., Séférian, R., Takao, S., Tatebe, H., Tian, H., Tilbrook, B., Torres, O., Tourigny, E., Tsujino, H., Tubiello, F., van der Werf, G., Wanninkhof, R., Wang, X., Yang, D., Yang, X., Yu, Z., Yuan, W., Yue, X., Zaehle, S., Zeng, N., and Zeng, J.: Global Carbon Budget 2024, Earth Syst. Sci. Data, 17, 965–1039, https://doi.org/10.5194/essd-17-965-2025, 2025.

Gaspari, G. and Cohn, S. E.: Construction of correlation functions in two and three dimensions, Quarterly Journal of the Royal Meteorological Society, 125, 723–757, https://doi.org/10.1002/qj.49712555417, 1999.

Gaudet, B. J., Davis, K. J., Pal, S., Jacobson, A. R., Schuh, A., Lauvaux, T., Feng, S., and Browell, E. V.: Regional-Scale, Sector-Specific Evaluation of Global CO_2 Inversion Models Using Aircraft Data From the ACT-America Project, Journal of Geophysical Research: Atmospheres, 126, e2020JD033623, https://doi.org/10.1029/2020JD033623, 2021.

Gregor, L. and Fay, A.: SeaFlux: harmonised sea-air CO2 fluxes from surface pCO_2 data products using a standardised approach (2021.04.03), [data set], https://doi.org/10.5281/zenodo.5482547 (last access: 22 October 2025), 2021.

Grell, G. A., Peckham, S. E., Schmitz, R., McKeen, S. A., Frost, G., Skamarock, W. C., and Eder, B.: Fully coupled "online" chemistry within the WRF model, Atmospheric Environment, 39, 6957–6975, https://doi.org/10.1016/j.atmosenv.2005.04.027, 2005.

Gurney, K. R., Law, R. M., Denning, A. S., Rayner, P. J., Baker, D., Bousquet, P., Bruhwiler, L., Chen, Y.-H., Ciais, P., Fan, S., Fung, I. Y., Gloor, M., Heimann, M., Higuchi, K., John, J., Maki, T., Maksyutov, S., Masarie, K., Peylin, P., Prather, M., Pak, B. C., Randerson, J., Sarmiento, J., Taguchi, S., Takahashi, T., and Yuen, C.-W.: Towards robust regional estimates of CO_2 sources and sinks using atmospheric transport models, Nature, 415, 626–630, https://doi.org/10.1038/415626a, 2002.

Harman, I. N.: The Role of Roughness Sublayer Dynamics Within Surface Exchange Schemes, Boundary-Layer Meteorol, 142, 1–20, https://doi.org/10.1007/s10546-011-9651-z, 2012.

Harman, I. N. and Finnigan, J. J.: A simple unified theory for flow in the canopy and roughness sublayer, Boundary-Layer Meteorol, 123, 339–363, https://doi.org/10.1007/s10546-006-9145-6, 2007.

Harman, I. N. and Finnigan, J. J.: Scalar Concentration Profiles in the Canopy and Roughness Sublayer, Boundary-Layer Meteorol, 129, 323–351, https://doi.org/10.1007/s10546-008-9328-4, 2008.

Henne, S., Brunner, D., Oney, B., Leuenberger, M., Eugster, W., Bamberger, I., Meinhardt, F., Steinbacher, M., and Emmenegger, L.: Validation of the Swiss methane emission inventory by atmospheric observations and inverse modelling, Atmospheric Chemistry and Physics, 16, 3683–3710, https://doi.org/10.5194/acp-16-3683-2016, 2016.

Hersbach, H., Bell, B., Berrisford, P., Biavati, G., Horányi, A., Muñoz Sabater, J., Nicolas, J., Peubey, C., Radu, R., Rozum, I., Schepers, D., Simmons, A., Soci, C., Dee, D., and Thépaut, J.-N.: ERA5 hourly data on pressure levels from 1959 to present, Copernicus Climate Change Service (C3S) Climate Data Store (CDS) [data set], https://doi.org/10.24381/cds.bd0915c6 (last access: 22 October 2025), 2023a.

Hersbach, H., Bell, B., Berrisford, P., Biavati, G., Horányi, A., Muñoz Sabater, J., Nicolas, J., Peubey, C., Radu, R., Rozum, I., Schepers, D., Simmons, A., Soci, C., Dee, D., and Thépaut, J.-N.: ERA5 hourly data on single levels from 1959 to present, Copernicus Climate Change Service (C3S) Climate Data Store (CDS) [data set], https://doi.org/10.24381/cds.adbb2d47 (last access: 22 October 2025), 2023b.

Hersbach, H., Bell, B., Berrisford, P., Hirahara, S., Horányi, A., Muñoz-Sabater, J., Nicolas, J., Peubey, C., Radu, R., Schepers, D., Simmons, A., Soci, C., Abdalla, S., Abellan, X., Balsamo, G., Bechtold, P., Biavati, G., Bidlot, J., Bonavita, M., De Chiara, G., Dahlgren, P., Dee, D., Diamantakis, M., Dragani, R., Flemming, J., Forbes, R., Fuentes, M., Geer, A., Haimberger, L., Healy, S., J. Hogan, R., Hólm, E., Janisková, M., Keeley, S., Laloyaux, P., Lopez, P., Lupu, C., Radnoti, G., de Rosnay, P., Rozum, I., Vamborg, F., Villaume, S., Thépaut, J.-N.: The ERA5 global reanalysis, Q. J. Roy. Meteor. Soc., 146, 1999-2049, https://doi.org/10.1002/qj.3803, 2020.

Hilton, T. W., Davis, K. J., Keller, K., and Urban, N. M.: Improving North American terrestrial CO_2 flux diagnosis using spatial structure in land surface model residuals, Biogeosciences, 10, 4607–4625, https://doi.org/10.5194/bg-10-4607-2013, 2013.

Hong, J. and Kim, J.: Impact of the Asian monsoon climate on ecosystem carbon and water exchanges: a wavelet analysis and its ecosystem modeling implications, Global Change Biology, 17, 1900–1916, https://doi.org/10.1111/j.1365-2486.2010.02337.x, 2011.

Hong, J.-W., Hong, J., Chun, J., Lee, Y. H., Chang, L.-S., Lee, J.-B., Yi, K., Park, Y.-S., Byun, Y.-H., and Joo, S.: Comparative assessment of net CO_2 exchange across an urbanization gradient in Korea based on eddy covariance measurements, Carbon Balance and Management, 14, 13, https://doi.org/10.1186/s13021-019-0128-6, 2019.

Hong, J.-W., Lee, S.-D., Lee, K., and Hong, J.: Seasonal variations in the surface energy and CO_2 flux over a high-rise, high-population, residential urban area in the East Asian monsoon region, International Journal of Climatology, 40, 4384–4407, https://doi.org/10.1002/joc.6463, 2020.

Hsu, C.-H., Henze, D. K., Mizzi, A. P., Abad, G. G., He, J., Harkins, C., Naeger, A. R., Lyu, C., Liu, X., Miller, C. C., Pierce, R. B., Johnson, M. S., and McDonald, B. C.: An Observing System Simulation Experiment Analysis of How Well Geostationary Satellite Trace-Gas Observations Constrain NOx Emissions in the US, Journal of Geophysical Research: Atmospheres, 129, e2023JD039323, https://doi.org/10.1029/2023JD039323, 2024.

Huang, Y., Wei, J., Jin, J., Zhou, Z., and Gu, Q.: CO Fluxes in Western Europe during 2017–2020 Winter Seasons Inverted by WRF-Chem/Data Assimilation Research Testbed with MOPITT Observations, Remote Sensing, 14, 1133, https://doi.org/10.3390/rs14051133, 2022.

Hutchins, M. G., Colby, J. D., Marland, G., and Marland, E.: A comparison of five high-resolution spatially-explicit, fossil-fuel, carbon dioxide emission inventories for the United States, Mitig Adapt Strateg Glob Change, 22, 947–972, https://doi.org/10.1007/s11027-016-9709-9, 2017.

Inness, A., Ades, M., Agustí-Panareda, A., Barré, J., Benedictow, A., Blechschmidt, A.-M., Dominguez, J. J., Engelen, R., Eskes, H., Flemming, J., Huijnen, V., Jones, L., Kipling, Z., Massart, S., Parrington, M., Peuch, V.-H., Razinger, M., Remy, S., Schulz, M., and Suttie, M.: The CAMS reanalysis of atmospheric composition, Atmospheric Chemistry and Physics, 19, 3515–3556, https://doi.org/10.5194/acp-19-3515-2019, 2019.

IPCC: Climate Change 2021: The Physical Science Basis. Contribution of Working Group I to the Sixth Assessment Report of the Intergovernmental Panel on Climate Change, edited by: Masson-Delmotte, V., Zhai, P., Pirani, A., Connors, S. L., Péan, C., Berger, S., Caud, N., Chen, Y., Goldfarb, L., Gomis, M. I., Huang, M., Leitzell, K., Lonnoy, E., Matthews, J. B. R., Maycock, T. K., Waterfield, T., Yelekçi, O., Yu, R., and Zhou, B., Cambridge University Press, https://doi.org/10.1017/9781009157896, 2021.

Janssens-Maenhout, G., Crippa, M., Guizzardi, D., Muntean, M., Schaaf, E., Dentener, F., Bergamaschi, P., Pagliari, V., Olivier, J. G. J., Peters, J. A. H. W., van Aardenne, J. A., Monni, S., Doering, U., Petrescu, A. M. R., Solazzo, E., and Oreggioni, G. D.: EDGAR v4.3.2 Global Atlas of the three major greenhouse gas emissions for the period 1970–2012, Earth System Science Data, 11, 959–1002, https://doi.org/10.5194/essd-11-959-2019, 2019.

Janssens-Maenhout, G., Pinty, B., Dowell, M., Zunker, H., Andersson, E., Balsamo, G., Bézy, J.-L., Brunhes, T., Bösch, H., Bojkov, B., Brunner, D., Buchwitz, M., Crisp, D., Ciais, P., Counet, P., Dee, D., Denier Van Der Gon, H., Dolman, H., Drinkwater, M. R., Dubovik, O., Engelen, R., Fehr, T., Fernandez, V., Heimann, M., Holmlund, K., Houweling, S., Husband, R., Juvyns, O., Kentarchos, A., Landgraf, J., Lang, R., Löscher, A., Marshall, J., Meijer, Y., Nakajima, M., Palmer, P. I., Peylin, P., Rayner, P., Scholze, M., Sierk, B., Tamminen, J., and Veefkind, P.: Toward an Operational Anthropogenic CO_2 Emissions Monitoring and Verification Support Capacity, Bulletin of the American Meteorological Society, 101, E1439–E1451, https://doi.org/10.1175/BAMS-D-19-0017.1, 2020.

Jiménez, P. A., Dudhia, J., González-Rouco, J. F., Navarro, J., Montávez, J. P., and García-Bustamante, E.: A Revised Scheme for the WRF Surface Layer Formulation, Monthly Weather Review, 140, 898–918, https://doi.org/10.1175/MWR-D-11-00056.1, 2012.

Jin, J., Huang, Y., Wei, C., Wang, X., Xu, X., Gu, Q., and Wang, M.: Analysis of CO_2 Concentration and Fluxes of Lisbon Portugal Using Regional CO_2 Assimilation Method Based on WRF-Chem, Atmosphere, 16, https://doi.org/10.3390/atmos16070847, 2025.

Jo, Y. H., Kim, S. H., Lee, Y. G., Kim, C. K., Hong, J., Lee, J., and Jang, K.: Evaluation of Topographic Effect Parameterizations in Weather Research and Forecasting Model over Complex Mountainous Terrain in Wildfire-Prone Regions, Fire, 8, https://doi.org/10.3390/fire8050196, 2025.

Jung, M., Henkel, K., Herold, M., and Churkina, G.: Exploiting synergies of global land cover products for carbon cycle modeling, Remote Sensing of Environment, 101, 534–553, https://doi.org/10.1016/j.rse.2006.01.020, 2006.

Kang, J.-S., Kalnay, E., Liu, J., Fung, I., Miyoshi, T., and Ide, K.: "Variable localization" in an ensemble Kalman filter: Application to the carbon cycle data assimilation, Journal of Geophysical Research: Atmospheres, 116, https://doi.org/10.1029/2010JD014673, 2011.

Kang, J.-S., Kalnay, E., Miyoshi, T., Liu, J., and Fung, I.: Estimation of surface carbon fluxes with an advanced data assimilation methodology, Journal of Geophysical Research: Atmospheres, 117, https://doi.org/10.1029/2012JD018259, 2012.

Kim, J., Shin, H.-J., Lee, K., and Hong, J.: Enhancement of ANN-based wind power forecasting by modification of surface roughness parameterization over complex terrain, Journal of Environmental Management, 362, 121246, https://doi.org/10.1016/j.jenvman.2024.121246, 2024.

Kwon, D., Hong, J., and Koo, B.: WRF-Chem/DART inversion system for CO_2 and CH_4 emissions in Korea, Zenodo [data set], https://doi.org/10.5281/zenodo.16939122 (last access: 15 October 2025), 2025a

Kwon, D., Hong, J., and Koo, B.: WRF-Chem/DART inversion dataset for CO_2 and CH_4 emissions in Korea, Zenodo [data set], https://doi.org/10.5281/zenodo.16947463 (last access: 15 October 2025), 2025b

Kwon, D., Hong, J., and Koo, B.: Data for: Regional CO2 and CH4 inversion system using WRF-Chem (v4.4)/DART (v9.8.0) and continuous high-precision observations over the Korean Peninsula, Zenodo [data set], https://doi.org/10.5281/zenodo.17402804 (last access: 24 October 2025), 2025c

Lauvaux, T., Miles, N. L., Deng, A., Richardson, S. J., Cambaliza, M. O., Davis, K. J., Gaudet, B., Gurney, K. R., Huang, J., O'Keefe, D., Song, Y., Karion, A., Oda, T., Patarasuk, R., Razlivanov, I., Sarmiento, D., Shepson, P., Sweeney, C., Turnbull, J., and Wu, K.: High-resolution atmospheric inversion of urban CO2 emissions during the dormant season of the Indianapolis Flux Experiment (INFLUX), Journal of Geophysical Research: Atmospheres, 121, 5213–5236, https://doi.org/10.1002/2015JD024473, 2016.

Lauvaux, T., Gurney, K. R., Miles, N. L., Davis, K. J., Richardson, S. J., Deng, A., Nathan, B. J., Oda, T., Wang, J. A., Hutyra, L., and Turnbull, J.: Policy-Relevant Assessment of Urban CO2 Emissions, Environ. Sci. Technol., 54, 10237–10245, https://doi.org/10.1021/acs.est.0c00343, 2020.

Lee, H., Han, S.-O., Ryoo, S.-B., Lee, J.-S., and Lee, G.-W.: The measurement of atmospheric CO2 at KMA GAW regional stations, its characteristics, and comparisons with other East Asian sites, Atmospheric Chemistry and Physics, 19, 2149–2163, https://doi.org/10.5194/acp-19-2149-2019, 2019.

Lee, H., Seo, W., Li, S., Lee, S., Kenea, S. T., and Joo, S.: Measurement report: Atmospheric CH_4 at regional stations of the Korea Meteorological Administration–Global Atmosphere Watch Programme: measurement, characteristics, and long-term changes of its drivers, Atmos. Chem. Phys., 23, 7141–7159, https://doi.org/10.5194/acp-23-7141-2023, 2023.

Lee, J. and Hong, J.: Implementation of spaceborne lidar-retrieved canopy height in the WRF model, Journal of Geophysical Research: Atmospheres, 121, 6863–6876, https://doi.org/10.1002/2015JD024299, 2016.

Lee, J., Hong, J., Noh, Y., and Jiménez, P. A.: Implementation of a roughness sublayer parameterization in the Weather Research and Forecasting model (WRF version 3.7.1) and its evaluation for regional climate simulations, Geoscientific Model Development, 13, 521–536, https://doi.org/10.5194/gmd-13-521-2020, 2020.

Lee, J., Shin, H. H., Hong, S.-Y., Jiménez, P. A., Dudhia, J., and Hong, J.: Impacts of subgrid-scale orography parameterization on simulated surface layer wind and monsoonal precipitation in the high-resolution WRF model, Journal of Geophysical Research: Atmospheres, 120, 644–653, https://doi.org/10.1002/2014JD022747, 2015.

Lee, J., Woo, H. J., Son, S.-K., Kim, M., Lee, D.-H., Tsunogai, U., and Jeong, K.-S.: Flux and distribution of methane (CH_4) in the Gunsan Basin of the southeastern Yellow Sea, off the Western Korea, Journal of Environmental Science and Health, Part A, 53, 457–466, https://doi.org/10.1080/10934529.2017.1409026, 2018.

Lee, J., Lee, H.-J., Kim, K.-B., Shin, H. H., Lim, J.-M., Hong, J., and Lim, K.-S. S.: Height correction method based on the Monin–Obukhov similarity theory for better prediction of near-surface wind fields, Atmospheric Research, 292, 106882, https://doi.org/10.1016/j.atmosres.2023.106882, 2023.

Lee, K., Hong, J.-W., Kim, J., and Hong, J.: Partitioning of net CO_2 exchanges at the city-atmosphere interface into biotic and abiotic components, MethodsX, 8, 101231, https://doi.org/10.1016/j.mex.2021.101231, 2021.

Li, X., Hu, X.-M., Cai, C., Jia, Q., Zhang, Y., Liu, J., Xue, M., Xu, J., Wen, R., and Crowell, S. M. R.: Terrestrial CO_2 Fluxes, Concentrations, Sources and Budget in Northeast China: Observational and Modeling Studies, Journal of Geophysical Research: Atmospheres, 125, e2019JD031686, https://doi.org/10.1029/2019JD031686, 2020.

Lim, K.-S. S., Lim, J.-M., Shin, H. H., Hong, J., Ji, Y.-Y., and Lee, W.: Impacts of subgrid-scale orography parameterization on simulated atmospheric fields over Korea using a high-resolution atmospheric forecast model, Meteorol Atmos Phys, 131, 975–985, https://doi.org/10.1007/s00703-018-0615-4, 2019.

Liu, X., Mizzi, A. P., Anderson, J. L., Fung, I., and Cohen, R. C.: Assimilation of satellite NO2 observations at high spatial resolution using OSSEs, Atmospheric Chemistry and Physics, 2017.

Ma, C., Wang, T., Jiang, Z., Wu, H., Zhao, M., Zhuang, B., Li, S., Xie, M., Li, M., Liu, J., and Wu, R.: Importance of Bias Correction in Data Assimilation of Multiple Observations Over Eastern China Using WRF-Chem/DART, Journal of Geophysical Research: Atmospheres, 125, e2019JD031465, https://doi.org/10.1029/2019JD031465, 2020.

Mahadevan, P., Wofsy, S. C., Matross, D. M., Xiao, X., Dunn, A. L., Lin, J. C., Gerbig, C., Munger, J. W., Chow, V. Y., and Gottlieb, E. W.: A satellite-based biosphere parameterization for net ecosystem CO_2 exchange: Vegetation Photosynthesis and Respiration Model (VPRM), Global Biogeochemical Cycles, 22, https://doi.org/10.1029/2006GB002735, 2008.

Michalak, A. M., Randazzo, N. A., and Chevallier, F.: Diagnostic methods for atmospheric inversions of long-lived greenhouse gases, Atmos. Chem. Phys., 17, 7405–7421, https://doi.org/10.5194/acp-17-7405-2017, 2017.

Ministry of Environment, Republic of Korea: The Republic of Korea's First Biennial Transparency Report and Fifth National Communication under the UNFCCC and the Paris Agreement, available at: https://unfccc.int/documents/645637 (last access: 06 June 2025), 2025.

Mizzi, A. P., Arellano Jr., A. F., Edwards, D. P., Anderson, J. L., and Pfister, G. G.: Assimilating compact phase space retrievals of atmospheric composition with WRF-Chem/DART: a regional chemical transport/ensemble Kalman filter data assimilation system, Geoscientific Model Development, 9, 965–978, https://doi.org/10.5194/gmd-9-965-2016, 2016.

Mizzi, A. P., Edwards, D. P., and Anderson, J. L.: Assimilating compact phase space retrievals (CPSRs): comparison with independent observations (MOZAIC in situ and IASI retrievals) and extension to assimilation of truncated retrieval profiles, Geoscientific Model Development, 11, 3727–3745, https://doi.org/10.5194/gmd-11-3727-2018, 2018.

Moon, J., Shim, C., Seo, J., and Han, J.: Evaluation of Korean methane emission sources with satellite retrievals by spatial correlation analysis, Environ Monit Assess, 196, 296, https://doi.org/10.1007/s10661-024-12449-w, 2024.

Mueller, K. L., Lauvaux, T., Gurney, K. R., Roest, G., Ghosh, S., Gourdji, S. M., Karion, A., DeCola, P., and Whetstone, J.: An emerging GHG estimation approach can help cities achieve their climate and sustainability goals, Environ. Res. Lett., 16, 084003, https://doi.org/10.1088/1748-9326/ac0f25, 2021.

Nalini, K., Lauvaux, T., Abdallah, C., Lian, J., Ciais, P., Utard, H., Laurent, O., and Ramonet, M.: High-Resolution Lagrangian Inverse Modeling of CO_2 Emissions Over the Paris Region During the First 2020 Lockdown Period, Journal of Geophysical Research: Atmospheres, 127, e2021JD036032, https://doi.org/10.1029/2021JD036032, 2022.

Nassar, R., Napier-Linton, L., Gurney, K. R., Andres, R. J., Oda, T., Vogel, F. R., and Deng, F.: Improving the temporal and spatial distribution of CO2 emissions from global fossil fuel emission data sets, Journal of Geophysical Research: Atmospheres, 118, 917–933, https://doi.org/10.1029/2012JD018196, 2013.

National Centers for Environmental Prediction, National Weather Service, NOAA, and U.S. Department of Commerce: NCEP ADP Global Upper Air and Surface Weather Observations (PREPBUFR format), Research Data Archive at the National Center for Atmospheric Research, Computational and Information Systems Laboratory [data set], https://doi.org/10.5065/Z83F-N512 (last access: 22 October 2025), 2008.

Nisbet, E. G., Manning, M. R., Dlugokencky, E. J., Fisher, R. E., Lowry, D., Michel, S. E., Myhre, C. L., Platt, S. M., Allen, G., Bousquet, P., Brownlow, R., Cain, M., France, J. L., Hermansen, O., Hossaini, R., Jones, A. E., Levin, I., Manning, A. C., Myhre, G., Pyle, J. A., Vaughn, B. H., Warwick, N. J., and White, J. W. C.: Very Strong Atmospheric Methane Growth in the 4 Years 2014–2017: Implications for the Paris Agreement, Global Biogeochemical Cycles, 33, 318–342, https://doi.org/10.1029/2018GB006009, 2019.

Oda, T. and Maksyutov, S.: ODIAC Fossil Fuel CO_2 Emissions Dataset (Version name: ODIAC2022), Center for Global Environmental Research, National Institute for Environmental Studies [data set], https://doi.org/10.17595/20170411.001 (last access: 22 October 2025), 2015.

Oda, T., Maksyutov, S., and Andres, R. J.: The Open-source Data Inventory for Anthropogenic CO_2, version 2016 (ODIAC2016): a global monthly fossil fuel CO_2 gridded emissions data product for tracer transport simulations and surface flux inversions, Earth System Science Data, 10, 87–107, https://doi.org/10.5194/essd-10-87-2018, 2018.

Oda, T., Bun, R., Kinakh, V., Topylko, P., Halushchak, M., Marland, G., Lauvaux, T., Jonas, M., Maksyutov, S., Nahorski, Z., Lesiv, M., Danylo, O., and Horabik-Pyzel, J.: Errors and uncertainties in a gridded carbon dioxide emissions inventory, Mitig Adapt Strateg Glob Change, 24, 1007–1050, https://doi.org/10.1007/s11027-019-09877-2, 2019.

Ogle, S. M., Buendia, L., Butterbach-Bahl, K., Breidt, F. J., Hartman, M., Yagi, K., Nayamuth, R., Spencer, S., Wirth, T., and Smith, P.: Advancing national greenhouse gas inventories for agriculture in developing countries: improving activity data, emission factors and software technology, Environ. Res. Lett., 8, 015030, https://doi.org/10.1088/1748-9326/8/1/015030, 2013.

Pauw, W. P., Klein, R. J. T., Mbeva, K., Dzebo, A., Cassanmagnago, D., and Rudloff, A.: Beyond headline mitigation numbers: we need more transparent and comparable NDCs to achieve the Paris Agreement on climate change, Climatic Change, 147, 23–29, https://doi.org/10.1007/s10584-017-2122-x, 2018.

Peng, Z., Zhang, M., Kou, X., Tian, X., and Ma, X.: A regional carbon data assimilation system and its preliminary evaluation in East Asia, Atmospheric Chemistry and Physics, 15, 1087–1104, https://doi.org/10.5194/acp-15-1087-2015, 2015.

Pisso, I., Patra, P., Takigawa, M., Machida, T., Matsueda, H., and Sawa, Y.: Assessing Lagrangian inverse modelling of urban anthropogenic CO_2 fluxes using in situ aircraft and ground-based measurements in the Tokyo area, Carbon Balance and Management, 14, 6, https://doi.org/10.1186/s13021-019-0118-8, 2019.

Pouyaei, A., Mizzi, A. P., Choi, Y., Mousavinezhad, S., and Khorshidian, N.: Downwind Ozone Changes of the 2019 Williams Flats Wildfire: Insights From WRF-Chem/DART Assimilation of OMI NO2, HCHO, and MODIS AOD Retrievals, Journal of Geophysical Research: Atmospheres, 128, e2022JD038019, https://doi.org/10.1029/2022JD038019, 2023.

Rayner, P. J., Raupach, M. R., Paget, M., Peylin, P., and Koffi, E.: A new global gridded data set of CO_2 emissions from fossil fuel combustion: Methodology and evaluation, Journal of Geophysical Research: Atmospheres, 115, https://doi.org/10.1029/2009JD013439, 2010.

Rogelj, J., Den Elzen, M., Höhne, N., Fransen, T., Fekete, H., Winkler, H., Schaeffer, R., Sha, F., Riahi, K., and Meinshausen, M.: Paris Agreement climate proposals need a boost to keep warming well below 2 °C, Nature, 534, 631–639, https://doi.org/10.1038/nature18307, 2016.

Roobaert, A., Laruelle, G. G., Landschützer, P., and Regnier, P.: Uncertainty in the global oceanic CO_2 uptake induced by wind forcing: quantification and spatial analysis, Biogeosciences, 15, 1701–1720, https://doi.org/10.5194/bg-15-1701-2018, 2018.

Roobaert, A., Laruelle, G. G., Landschützer, P., Gruber, N., Chou, L., and Regnier, P.: The Spatiotemporal Dynamics of the Sources and Sinks of CO_2 in the Global Coastal Ocean, Global Biogeochemical Cycles, 33, 1693–1714, https://doi.org/10.1029/2019GB006239, 2019.

Schroeder, W., Oliva, P., Giglio, L., and Csiszar, I. A.: The New VIIRS 375 m active fire detection data product: Algorithm description and initial assessment, Remote Sensing of Environment, 143, 85–96, https://doi.org/10.1016/j.rse.2013.12.008, 2014.

Segato, D., Graziosi, F., and Manca, G.: Evaluation of Copernicus atmosphere monitoring service methane products 2019-2023, Publications Office of the European Union, https://data.europa.eu/doi/10.2760/8653047, 2025.

Shim, C., Han, J., Henze, D. K., and Yoon, T.: Identifying local anthropogenic CO_2 emissions with satellite retrievals: a case study in South Korea, International Journal of Remote Sensing, 40, 1011–1029, https://doi.org/10.1080/01431161.2018.1523585, 2019.

Sijikumar, S., Raju, A., Valsala, V., Tiwari, Y., Girach, I. A., Jain, C. D., and Ratnam, M. V.: High-Resolution Bayesian Inversion of Carbon Dioxide Flux Over Peninsular India, Atmospheric Environment, 308, 119868, https://doi.org/10.1016/j.atmosenv.2023.119868, 2023.

Super, I., Denier van der Gon, H. A. C., van der Molen, M. K., Sterk, H. A. M., Hensen, A., and Peters, W.: A multi-model approach to monitor emissions of CO_2 and CO from an urban–industrial complex, Atmospheric Chemistry and Physics, 17, 13297–13316, https://doi.org/10.5194/acp-17-13297-2017, 2017.

UNFCCC: Adoption of the Paris Agreement. Report No. FCCC/CP/2015/L.9/ Rev.1, available at: https://unfccc.int/resource/docs/2015/cop21/eng/l09r01.pdf (last access: 22 October 2025), 2015.

Velasco, E., Segovia, E., and Roth, M.: High-resolution maps of carbon dioxide and moisture fluxes over an urban neighborhood, Environ. Sci.: Atmos., 3, 1110–1123, https://doi.org/10.1039/D2EA00108J, 2023.

Wang, Y., Yuan, Q., Li, T., Yang, Y., Zhou, S., and Zhang, L.: Seamless mapping of long-term (2010-2020) daily global XCO_2 and XCH_4 from the Greenhouse Gases Observing Satellite (GOSAT), Orbiting Carbon Observatory 2 (OCO-2), and CAMS global greenhouse gas reanalysis (CAMS-EGG4) with a spatiotemporally self-supervised fusion method, Earth System Science Data, 15, 3597-3622, https://doi.org/10.5194/essd-15-3597-2023, 2023.

Weber, T., Wiseman, N. A., and Kock, A.: Global ocean methane emissions dominated by shallow coastal waters, Nat Commun, 10, 4584, https://doi.org/10.1038/s41467-019-12541-7, 2019.

Weiss, R. F. and Prinn, R. G.: Quantifying greenhouse-gas emissions from atmospheric measurements: a critical reality check for climate legislation, Philosophical Transactions of the Royal Society A: Mathematical, Physical and Engineering Sciences, 369, 1925–1942, https://doi.org/10.1098/rsta.2011.0006, 2011.

Wiedinmyer, C. and Emmons, L.: Fire Inventory from NCAR version 2 Fire Emission. Research Data Archive at the National Center for Atmospheric Research, Computational and Information Systems Laboratory [data set], https://doi.org/10.5065/XNPA-AF09 (last access: 22 October 2025), 2022.

Wiedinmyer, C., Akagi, S. K., Yokelson, R. J., Emmons, L. K., Al-Saadi, J. A., Orlando, J. J., and Soja, A. J.: The Fire INventory from NCAR (FINN): a high resolution global model to estimate the emissions from open burning, Geoscientific Model Development, 4, 625–641, https://doi.org/10.5194/gmd-4-625-2011, 2011.

Wiedinmyer, C., Kimura, Y., McDonald-Buller, E. C., Emmons, L. K., Buchholz, R. R., Tang, W., Seto, K., Joseph, M. B., Barsanti, K. C., Carlton, A. G., and Yokelson, R.: The Fire Inventory from NCAR version 2.5: an updated global fire emissions model for climate and chemistry applications, Geoscientific Model Development, 16, 3873–3891, https://doi.org/10.5194/gmd-16-3873-2023, 2023.

WMO: IG3IS Urban Greenhouse Gas Emission Observation and Monitoring Good Research Practice Guidelines, WMO GAW Report No 275, available at: https://library.wmo.int/idurl/4/58055, 2022.

WMO: Integrated Global Greenhouse Gas Information System Good Practice Guidance for Estimating National-scale Greenhouse Gas Emissions using Atmospheric Observations, WMO GAW Report No. 319, available at: https://library.wmo.int/idurl/4/69714, 2025.

Zhang, Q., Li, M., Wang, M., Mizzi, A. P., Huang, Y., Wei, C., Jin, J., and Gu, Q.: CO_2 Flux over the Contiguous United States in 2016 Inverted by WRF-Chem/DART from OCO-2 XCO2 Retrievals, Remote Sensing, 13, 2996, https://doi.org/10.3390/rs13152996, 2021a.

Zhang, Q., Li, M., Wei, C., Mizzi, A. P., Huang, Y., and Gu, Q.: Assimilation of OCO-2 retrievals with WRF-Chem/DART: A case study for the Midwestern United States, Atmospheric Environment, 246, 118106, https://doi.org/10.1016/j.atmosenv.2020.118106, 2021b.

Zhang, Z., Poulter, B., Melton, J. R., Riley, W. J., Allen, G. H., Beerling, D. J., Bousquet, P., Canadell, J. G., Fluet-Chouinard, E., Ciais, P., Gedney, N., Hopcroft, P. O., Ito, A., Jackson, R. B., Jain, A. K., Jensen, K., Joos, F., Kleinen, T., Knox, S. H., Li, T., Li, X., Liu, X., McDonald, K., McNicol, G., Miller, P. A., Müller, J., Patra, P. K., Peng, C., Peng, S., Qin, Z., Riggs, R. M., Saunois, M., Sun, Q., Tian, H., Xu, X., Yao, Y., Xi, Y., Zhang, W., Zhu, Q., Zhu, Q., and Zhuang, Q.: Ensemble estimates of global wetland methane emissions over 2000–2020, Biogeosciences, 22, 305–321, https://doi.org/10.5194/bg-22-305-2025, 2025.

Zhao, X., Chen, J., Marshall, J., Gałkowski, M., Hachinger, S., Dietrich, F., Shekhar, A., Gensheimer, J., Wenzel, A., and Gerbig, C.: Understanding greenhouse gas (GHG) column concentrations in Munich using the Weather Research and Forecasting (WRF) model, Atmospheric Chemistry and Physics, 23, 14325–14347, https://doi.org/10.5194/acp-23-14325-2023, 2023.

Zhao, Y., Saunois, M., Bousquet, P., Lin, X., Berchet, A., Hegglin, M. I., Canadell, J. G., Jackson, R. B., Dlugokencky, E. J., Langenfelds, R. L., Ramonet, M., Worthy, D., and Zheng, B.: Influences of hydroxyl radicals (OH) on top-down estimates of the global and regional methane budgets, Atmospheric Chemistry and Physics, 20, 9525–9546, https://doi.org/10.5194/acp-20-9525-2020, 2020.